The Depositional Record
The journal of the International Association of Sedimentologists
Open Access

ORIGINAL RESEARCH ARTICLE

Disentangling shallow-water bulk carbonate carbon isotope archives with evidence for multi-stage diagenesis: An in-depth component-specific petrographic and geochemical study from Oman (mid-Cretaceous)

STEFAN HUCK*, STEPHAN WOHLWEND†, RUTE COIMBRA‡,§ NICOLAS CHRIST¶ and HELMUT WEISSERT†

*Institut für Geologie, Leibniz Universität Hannover, Callinstraße 30, D-30167 Hannover, Germany (E-mail: huck@geowi.uni-hannover.de)
†Geological Institute, ETH Zürich, CH-8004 Zürich, Switzerland
‡Department of Geosciences, GeoBioTec, University of Aveiro, PT-3810-193 Aveiro, Portugal
§Earth Sciences Department, MARE, University of Coimbra, PT-3030-790 Coimbra, Portugal
¶Institute of Earth and Environmental Science, University of Potsdam, K.-Liebknecht-Str. 24, D-14476 Potsdam-Golm, Germany

Keywords
Arabian carbonate platform, Barremian–Aptian, multi-stage diagenesis, shallow-water chemostratigraphy.

Manuscript received: 20 June 2017;
Accepted: 28 August 2017

The Depositional Record 2017; 3(2): 233–257

doi: 10.1002/dep2.35

ABSTRACT

Disentangling shallow-water bulk carbonate carbon isotope archives into primary and diagenetic components is a notoriously difficult task and even diagenetically screened records often provide chemostratigraphic patterns that significantly differ from global signals. This is mainly caused by the polygenetic nature of shallow-water carbonate substrates, local carbon cycle processes causing considerable neritic–pelagic isotope gradients and the presence of hiatal surfaces resulting in extremely low carbonate preservation rates. Provided here is an in-depth petrographic and geochemical evaluation of different carbonate phases of a mid-Cretaceous (Barremian–Aptian) shallow-water limestone succession (Jabal Madar section) deposited on the tropical Arabian carbonate platform in Oman. The superposition of stable isotope signatures of identified carbonate phases causes a complex and often noisy bulk carbon isotope pattern. Blocky sparite cements filling intergranular pores and bioclastic voids evidence intermediate to (arguably) deep burial diagenetic conditions during their formation, owing to different timing or differential faulting promoting the circulation of fluids from variable sources. In contrast, sparite cements filling sub-vertical veins reveal a rock-buffered diagenetic fluid composition with an intriguing moderate enrichment in ^{13}C, probably due to fractionation during pressure release in the context of the Miocene exhumation of the carbonate platform under study. The presence of abundant, replacive dedolomite in mud-supported limestone samples forced negative carbon and oxygen isotope changes that are either associated with the thermal breakdown of organic matter in the deep burial realm or the expulsion of buried meteoric water in the intermediate burial realm. Notwithstanding the documented stratigraphically variable and often facies-related impact of different diagenetic fluids on the bulk-rock stable isotope signature, the identification of diagenetic end-members defined $\delta^{13}C$ and $\delta^{18}O$ threshold values that allowed the most reliable 'primary' bulk carbon isotope signatures to be extracted. Most importantly, this approach exemplifies how to place regional shallow-water stable isotope patterns with evidence for a complex multi-stage diagenetic history into a supraregional or even global context.

INTRODUCTION

Shallow-water carbon isotope variations recorded by bulk carbonate material have been proven to provide well-defined tie points for the correlation of deep-time carbonate platform sections and has further been used to stratigraphically link major changes in biosedimentation (biotic turnovers, carbonate platform demise and drowning) to climate and palaeoenvironmental changes associated with major carbon cycle perturbations (Föllmi *et al.*, 1994, 2006; Ferreri *et al.*, 1997; Grötsch *et al.*, 1998; Wissler *et al.*, 2002; Immenhauser *et al.*, 2005; Parente *et al.*, 2007; Burla *et al.*, 2008; Frijia & Parente, 2008; Elrick *et al.*, 2009; Millán *et al.*, 2009, 2011; El-Sabbagh *et al.*, 2011; Huck *et al.*, 2011, 2013, 2014; Di Lucia *et al.*, 2012; Krencker *et al.*, 2014; Bodin *et al.*, 2015; Wohlwend *et al.*, 2016). Unfortunately, the carbon isotope-based stratigraphic refinement of biostratigraphically poorly constrained shallow-water sections is often afflicted with large uncertainties unless additional stratigraphic methods such as strontium isotope stratigraphy (SIS) are applied (Huck *et al.*, 2010, 2011; Horikx *et al.*, 2014; Frijia *et al.*, 2015; Huck & Heimhofer, 2015; Bover-Arnal *et al.*, 2016). Without a proper SIS framework, shallow-water carbon isotope stratigraphy is solely based on the correlation of similar fluctuations ('wiggle matching') within a dating uncertainty (Weissert *et al.*, 2008). This is particularly problematic, as the shallow-water carbon isotope pool of dissolved inorganic carbon (DIC) is affected to varying degrees by (i) local carbon cycle processes, (ii) syn-depositional diagenesis and (ii) fractionation effects associated with varying contributions of aragonite, low-magnesium and high-magnesium calcite (Immenhauser *et al.*, 2002, 2008). Moreover, the shape of shallow-water carbon isotope curves is strongly modulated by sea-level fluctuations, as subaerial exposure and re-flooding of the platform causes phases of non-deposition, erosion, reworking and bypass of sediments. As a consequence, up to 90% of the carbon isotope signal may be lost in discontinuity surfaces or condensed in thin sedimentary layers (Strasser, 2015) and thus 'wiggle matching' between carbon isotope curves with locally different absolute values, amplitudes and gradients of excursions will allow multiple stratigraphic interpretations (Weissert *et al.*, 2008).

The current study aims at exemplifying how to extract stratigraphically meaningful global carbon cycle fluctuations out of shallow-water bulk carbonate carbon isotope archives that show evidence for a complex multi-stage diagenetic alteration. Therefore, a detailed sedimentological, petrographic and geochemical approach has been applied to a mid-Cretaceous southern Tethyan Arabian carbonate platform section (Jabal Madar) in Oman (Fig. 1A). The Jabal Madar section has been chosen as an ideal case study, as numerous biostratigraphic and sequence stratigraphic tie points are available (van Buchem *et al.*, 2002; Pittet *et al.*, 2002; Schröder *et al.*, 2010), but the stratigraphic resolution, in particular with respect to the Barremian interval, is rather low. Owing to previous work (van Buchem *et al.*, 2002; Pittet *et al.*, 2002), the studied limestone succession exposed at the Jabal Madar dome evidently suffered strong multi-stage diagenetic alteration in the eogenetic, mesogenetic and telogenetic realms (mud cracks, rhizoliths, stylolites, dolomite). Notably, the (compacted) carbonate 'preservation rate' *sensu* Strasser (2015) for the Barremian portion of the Jabal Madar section (calculated from Pittet *et al.*, 2002) is low (0·012 mm y^{-1}), an observation that clearly highlights the dominance of phases of sediment starvation and/or removal.

The overall aim of this study is thus to disentangle the local bulk carbonate carbon and oxygen isotope pattern, that is, to evaluate the influence of (i) local carbon cycling processes and (ii) syn to post-depositional diagenesis on the $\delta^{13}C_{bulk}$ record. Therefore, a component-specific comparison of carbon and oxygen isotope values is applied in order to define isotopic end-members representing specific diagenetic realms. In combination with an in-depth sedimentological, petrographic and elemental geochemistry inspection, a precise evaluation of the chemostratigraphic potential of the carbon isotope record is possible (Fig. 2). This will in turn allow a more objective correlation of the Jabal Madar $\delta^{13}C_{bulk}$ record with local carbon isotope patterns representing different settings of the Arabian carbonate platform and thus, the integration of valuable stratigraphic information on a platform-wide scale. Based on this integrated chemostratigraphic, sequence stratigraphic and biostratigraphic framework, the Jabal Madar section can be placed against stratigraphically well-constrained Tethyan neritic and pelagic sections. The outcome of this study will help to better attribute Tethyan-wide major steps in carbonate platform evolution (e.g. orbitolinid mass occurrences) to their corresponding palaeoenvironmental and palaeoceanographic forcing mechanisms.

GEOLOGICAL SETTING

The Jabal Madar dome is located in the Adam Foothills of northern Oman, about 140 km south of Muscat and about 5 km east of 'Uyun (Fig. 1B). The base of the studied Jabal Madar section is situated in the eastern part of the dome (22°23′14·79″N/58°10′03·65″E). The section comprises Barremian to Aptian carbonate platform deposits belonging to the Lekhwair, Kharaib and Shu'aiba

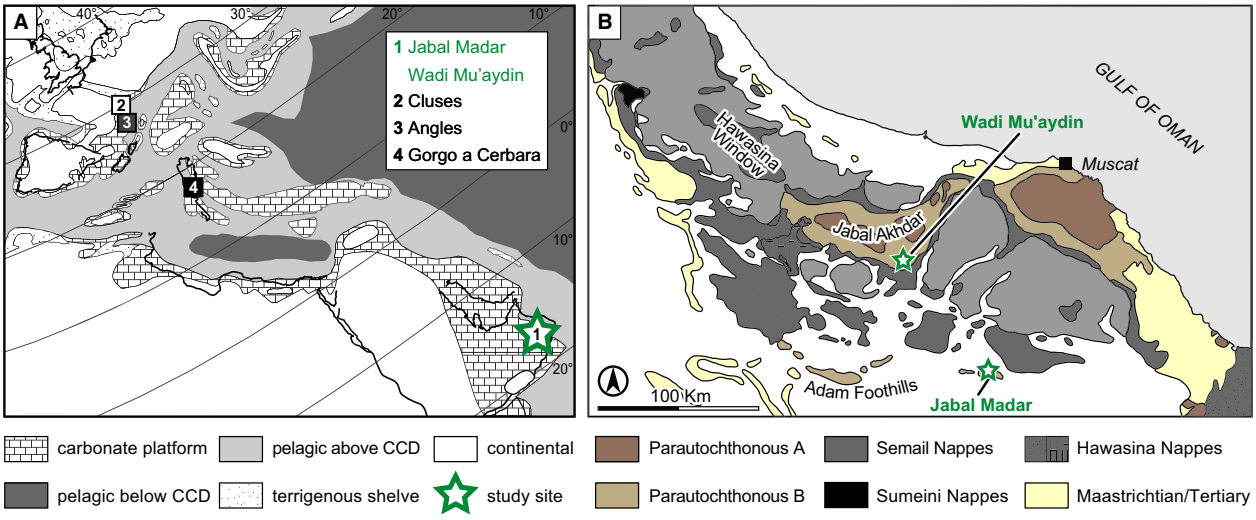

Fig. 1. (A) Aptian palaeogeography of the Tethyan realm with localities of considered pelagic (Angles, Gorgo a Cerbara) and neritic (Jabal Madar, Cluses) sections. Map is modified after Masse *et al.* (1998b). (B) Simplified geological map of north-eastern Oman showing the geographic position of the studied Jabal Madar section in the Adam Foothills and the Wadi Mu'aydin section at Jabal Akhtar. Adapted from Glennie *et al.* (1974) and modified after Wohlwend *et al.* (2017).

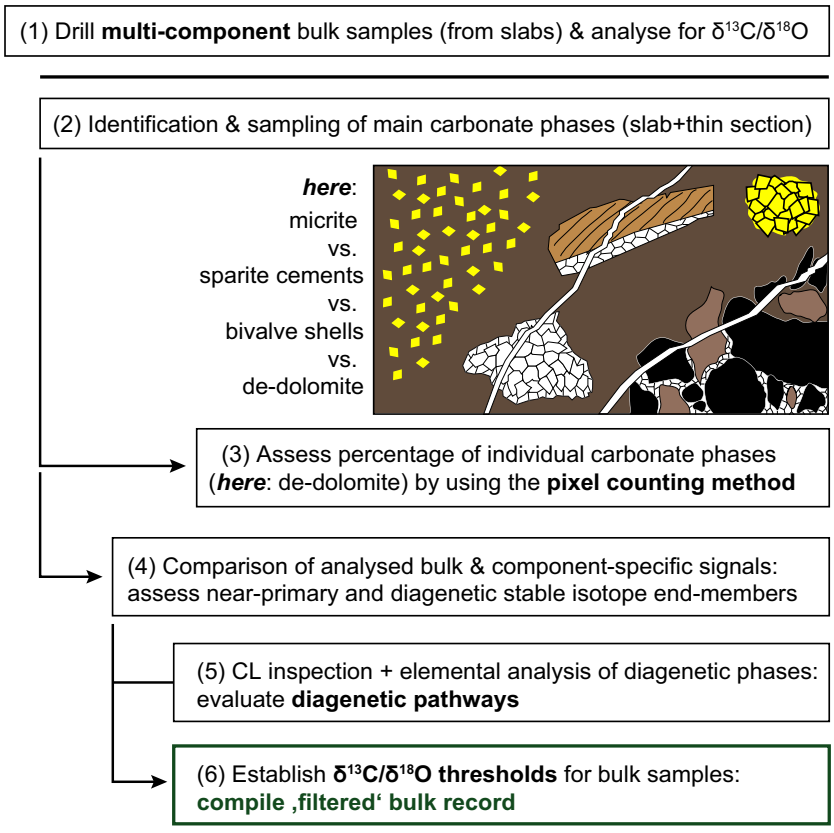

Fig. 2. Flow chart illustrating the here applied diagenetic screening protocol that builds on a component-specific petrographic and geochemical approach. This approach allows shallow-water bulk carbonate carbon isotope records with evidence for a multi-stage diagenetic alteration to be evaluated.

formations (Wilson, 1969; Glennie *et al.*, 1974; Pittet *et al.*, 2002). The latter have been deposited in very shallow lagoonal environments on the Arabian carbonate platform in a tropical southern Tethyan setting (*ca* 19°S: van Hinsbergen *et al.*, 2015) and belong to the so-called autochthonous Mesozoic carbonate successions of the Arabian Plate (Glennie *et al.*, 1974; Simmons & Hart, 1987). During Late Cretaceous ophiolite obduction, the mid-Cretaceous deposits of the Adam Foothills experienced burial depths of up to 4 km (Hanna, 1990; Mozafari *et al.*, 2015). Miocene uplift and deformation processes caused the exhumation of the Lower Cretaceous succession (Beurrier *et al.*, 1986; Le Metour *et al.*, 1986; Hanna, 1990; Fournier *et al.*, 2006).

In the Oman Mountains, the 65 to 120 m thick, medium to thickly bedded Lekhwair Formation is characterized by bioclastic wackestones and packstones and intercalated intraclastic and oolitic grainstones and packstones (Simmons & Hart, 1987; Simmons, 1990). Common sedimentary features include cross-bedding, channel structures, tempestites, cryptalgal laminates and (often dolomitized) burrows. The fossil content comprises allochthonous macrofauna (oysters, rudists, gastropods and subordinately large corals and stromatoporoids) as well as abundant dasycladacean algae and larger foraminifera (Simmons & Hart, 1987; Simmons, 1990). The 40 to 120 m thick Kharaib Formation is characterized by a cyclic alternation of massive wackestone–packstone–grainstone and argillaceous orbitolinid-rich wackestone–packstone units, which grade upwards into burrowed mudstones (Simmons, 1990; van Buchem *et al.*, 2002; Pittet *et al.*, 2002; Hillgärtner *et al.*, 2003). In general, bioturbation and stylolitization is common. Besides the transient mass occurrence of the orbitolinid foraminifera *Palorbitolina lenticularis*, calcareous algae, other benthic foraminifers, corals, rudists and other molluscs are occasionally present (Simmons & Hart, 1987; Simmons, 1990; Masse *et al.*, 1998b). The up to 100 m thick, massively bedded Shu'aiba Formation (Witt & Gökdag, 1994; Masse *et al.*, 1998a,b; Sharland *et al.*, 2001; van Buchem *et al.*, 2002; Rameil *et al.*, 2012) comprises bioclastic, often bioturbated mudstones and wackestones, foraminiferal–peloidal packstones–grainstones as well as floatstones and boundstones dominated by *Lithocodium–Bacinella* microencrusters. Caprinid rudist biostromes are a diagnostic feature of the upper part of the formation (Simmons & Hart, 1987; Simmons, 1990; Masse *et al.*, 1998a).

A detailed sedimentological, sequence stratigraphic and cyclostratigraphic study of the Lekhwair, Kharaib and Shu'aiba formations exposed at the Jabal Madar dome is presented in Pittet *et al.* (2002).

FIELD APPROACHES AND LABORATORY METHODS

The working approach used for sedimentological characterization of the 74 m thick Jabal Madar section involved an outcrop-based carbonate facies description, supported by the petrographic analysis of 73 thin sections. Microfacies analysis followed the limestone classification scheme of Dunham (1962), including the modifications by Embry & Klovan (1971), and is based on a component analysis (including biostratigraphically meaningful microfossils) and on textural and diagenetic features. The percentage of individual carbonate phases including sparite cements and dedolomite rhombs present in selected thin sections (i.e. microphotographs) was estimated by applying the pixel counting method *sensu* Coimbra & Olóriz (2012a). Samples for geochemical investigations were taken at a spacing of 0·3 to 1·5 m (mean: 0·7 m). Higher sample densities were applied across facies boundaries and discontinuity surfaces.

Carbonate powders were extracted from carbonate slabs by means of a hand-held PROXXON IBS/E drill equipped with tungsten drill bits (maximum speed: 8000 rpm). In order to evaluate the intra-sample variability in the bulk carbonate carbon and oxygen isotope composition (Fig. 2), several subsamples were drilled from about 50% (n = 52) of all collected hand specimens (n = 115). In addition, sampling focused on the extraction of powders from the main carbonate phases identified at thin section scale. These include (i) diagenetic (dedolomitized limestone; sparite cement filling intergranular pore space, veinlets and voids) as well as (ii) near-primary carbonate phases (matrix micrite *sensu stricto*, low-Mg calcite bivalve shell fragments). In total, carbon and oxygen isotope analysis of 383 carbonate powder samples (bulk: n = 202; matrix micrite: n = 43; dedolomitized limestone: n = 36; sparite cement: n = 87; bivalves: n = 15) was performed at the isotope laboratories of the Institute of Geology at Leibniz University Hannover (LUH), Germany (Tables SI-1/2). Stable isotope analysis was conducted using a Thermo Fisher Scientific Gasbench II carbonate device connected to a Thermo Fisher Scientific Delta-V Advantage isotope ratio mass spectrometer. Aliquots of the samples (200 ± 30 μg) were treated with viscous water-free (98 g mol^{-1}) orthophosphoric acid at 72°C to release CO_2. In order to ensure that samples containing variable amounts of dolomite have proper equilibration times (>2 h) with the acid, the latter is injected manually before the start of the measurement. Repeated analyses of certified carbonate standards (NBS 19, NBS-18, IAEA CO-1) show an external reproducibility of ≤0·06‰ for $\delta^{13}C$ and 0·08‰ for $\delta^{18}O$. All isotope results are reported in per

mil (‰) relative to the Vienna-Pee Dee Formation belemnite (V-PDB) standard in the conventional manner. For chemostratigraphic correlation, a three-point moving average was calculated. Oxygen isotope ratios, plotted against carbon isotope ratios, are used as proxy for the impact of diagenetic alteration.

At the isotope laboratory of the Institute of Geology, Mineralogy and Geophysics at Ruhr-University Bochum (RUB), Germany, aliquots (1·35 to 1·65 mg) of 26 powdered subsamples (matrix micrite: $n = 10$; grainstone bulk carbonate: $n = 5$; sparite cement: $n = 6$; dedolomite-rich limestones: $n = 3$; bivalves: $n = 3$) were analysed for their major and trace elemental composition (calcium, magnesium, strontium, iron and manganese) using inductively coupled plasma-atomic emission spectrometry (ICP-AES). Strontium isotope ratios of selected subsamples (matrix micrite: $n = 4$; bivalve: 1) were measured at RUB by means of a thermal ionization mass spectrometer (Finnigan MAT 262) in dynamic mode. Corrections of measured strontium isotope ratios to a USGS EN-1 value of 0·709175 were done following the procedure of Howarth & McArthur (1997). For more details on the analytical procedure please refer to Huck *et al.* (2011).

In addition, cathodoluminescence (CL) examination of 12 thin sections was carried out with a "hot cathode" CL microscope (type HC1-LM) at Potsdam University. The acceleration voltage of the electron beam is 14 kV and the beam current is set to a level gaining a current density of *ca* 9 μA mm^{-2} on the sample surface. Refer to Christ *et al.* (2012) for details on the analytical procedure.

LITHOSTRATIGRAPHY AND MICROFACIES OF THE JABAL MADAR SECTION

The studied 74 m thick Barremian portion of the shallow-water Jabal Madar section (total thickness: 111·6 m; Pittet *et al.*, 2002; Sattler *et al.*, 2005) is dominated by restricted to open lagoonal fine-grained limestones with intercalations of coarse-grained partly cross-bedded, as well as slightly argillaceous orbitolinid-rich levels (Figs 3A and 4, Table 1). Dedolomitization is rather common and predominantly affects matrix micrites, burrow-infills and, to a lesser extent, cement-filled veinlets, micro-stylolites and voids. At thin section scale, dedolomitized samples mainly exhibit planar-euhedral, planar-subhedral and planar-porphyrotopic textures (calcified rhombs: 45 to 85 μm in diameter; Fig. 3C) and subordinately microcrystalline non-planar anhedral or macrocrystalline void-filling irregular textures. Pixel counting applied to microphotographs (Coimbra & Olóriz, 2012a) revealed dedolomite contents ranging from 5% to 95% (Table SI-3). Drusy calcite filling voids and fractures is a common feature of the lower two-third of the section (0 to 49 m), whereas the upper part (53 to 74 m) is characterized by whitish, mud-dominated limestones with a chalky (microporous) appearance.

The lowermost part of the section (0 to 16 m; Fig. 4) is composed of an alternation of peloidal–foraminiferal packstones and grainstones (microfacies type MFT-1) and yellowish-brownish to dark grey mudstones and wackestones containing variable but overall minor proportions of gastropods, ostracods, sponge spicules, echinoderms, benthic foraminifers, dasycladacean algae and peloids (MFT-4/5). Stratigraphic marker levels include two reddish-weathering dedolomite beds with a thickness of up to 0·5 m (4·7 m; 11·1 m; MFT-8; Fig. 3B) and a thin burrowed firmground (8 m; Fig. 3D). A succession of often cross-bedded grainstones, rudstones and subordinate peloidal packstones characterizes the overlying deposits (16 to 24 m; MFT-1/2), which contain various allochems including partly silicified bivalve fragments (e.g. rudists), intraclasts, faecal pellets, benthic foraminifers and green algae (e.g. *Coptocampylodon lineolatus* and calcitic *Hensonella dinarica*). Upsection, this calcarenitic unit is truncated by a succession of alternating gastropod-echinoderm-algal mudstones and wackestones and subordinate peloidal packstones (24 to 40 m; MFT-1/4/5). Stratigraphic marker levels include decimetre-thick reddish-weathering dedolomite beds (26 m; 30·3 m; 36·1 m; MFT-8), a 2 m thick nodular level capped by a hardground (34·2 m; Fig. 3E) and an interval characterized by abundant partly dolomitized *Thalassinoides* burrows (36 to 40 m).

The following lithostratigraphic unit is composed of peloidal–foraminiferal to bioclastic packstones and grainstones to rudstones (40 to 43 m; MFT-1/2). These high-energy deposits are overlain by a succession (43 to 53 m) of slightly argillaceous wackestones and packstones bearing abundant orbitolinids (*P. lenticularis*, *Eopalorbitolina transiens*) and echinoderm fragments (Fig. 3F; MFT-6/7) and bioclastic mudstones/wackestones and packstones; MF-type 4), the latter being characterized by yellowish dolomitized *Thalassinoides* burrows (e.g. 45·9 m; Fig. 3G). A decimetre-thick grainstone to rudstone interval containing bacinelloid oncoids (51 m; MFT-3, cf. Huck *et al.*, 2012) is intercalated in the topmost considerably bioturbated (*Thalassinoides*) part of this unit (51 to 53 m). The following whitish-weathering 'chalky' unit (53 to 74 m) comprises often bioturbated echinoderm-orbitolinid mudstones and mudstones/wackestones (with *Montseciella arabica* and *P. lenticularis*; MFT-7) characterized by a stratigraphically limited moderate to strong intraparticle porosity (dissolution of dedolomite rhombs) and a centimetre-thick brecciated mudstone level at 68·8 m. The upper boundary of the

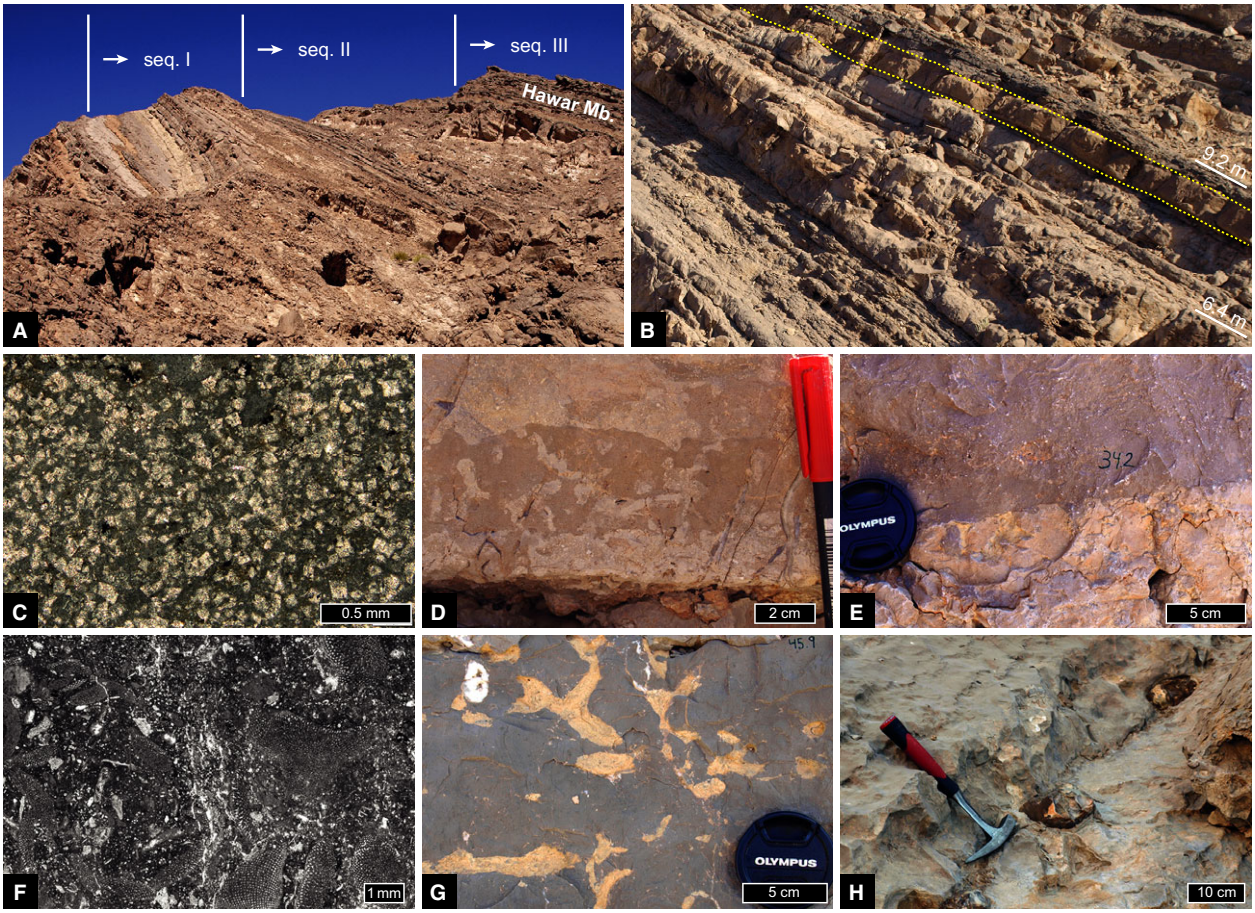

Fig. 3. Field and thin section pictures documenting the stacking pattern, major bio-sedimentary changes and diagenetic features of limestones exposed at the eastern flank of the Jabal Madar dome. (A) Alternation of thinly bedded and more massive intervals referred to as sequences I to III (van Buchem *et al.*, 2002; Pittet *et al.*, 2002). Note reddish dedolomite bed at the base of sequence I and orbitolinid-rich slightly argillaceous limestones at the base of sequence II and III (Hawar Member). (B) Prominent reddish dedolomite bed (dashed stippled line) exposed at lower part of the Jabal Madar section. Sample JM8.6 (C) Microphotograph of replacive dedolomite with planar-porphyrotopic texture. MFT-8, sample JM47.7. (D) Thin burrowed firmground at 8 m. (E) Hardground with spherical borings at 34·2 m. (F) Slightly argillaceous and dedolomitized orbitolinid-(echinoderm) packstone, MFT-6, sample JM48.4. (G) Yellowish dedolomitized *Thalassinoides* burrows within dark grey mudstone matrix at 45·9 m. (H) Layer of roundish to elongate chert nodules marking the top (74 m) of the studied portion of the Jabal Madar section.

studied portion of the Jabal Madar section (74 m) is marked by a level of layered chert nodules (<5 to 10 cm in diameter; Fig. 3H) at the base of a predominantly grain-supported interval (74 to 80·5 m). Following Sattler *et al.* (2005), a prominent composite surface (CS1; Fig. 4) marks the transition into the slightly argillaceous orbitolinid-rich limestones (80·5 to 101 m) referred to as the Hawar Member (van Buchem *et al.*, 2002; Pittet *et al.*, 2002), which are overlain by *Lithocodium-Bacinella* grainstones and floatstones of the Lower Shu'aiba Formation (101 to 111·6 m). For more details on the microfacies and fossil content of Jabal Madar samples please refer to Table 1.

GEOCHEMICAL AND PETROGRAPHIC RESULTS

Bulk carbonate carbon and oxygen isotope stratigraphy

The bulk carbonate carbon isotope ($\delta^{13}C_{bulk}$) record of the Jabal Madar section (Fig. 4) is characterized by numerous alternating negative and positive changes, with $\delta^{13}C_{bulk}$ values ranging between −2·8‰ and 3·6‰ (mean: 1·2‰; SD: 1·4‰). In general, the lower part of the section (0 to 37·4 m) shows stronger oscillations and overall lowered $\delta^{13}C_{bulk}$ values (mean: 0·4‰; SD: 1·3‰)

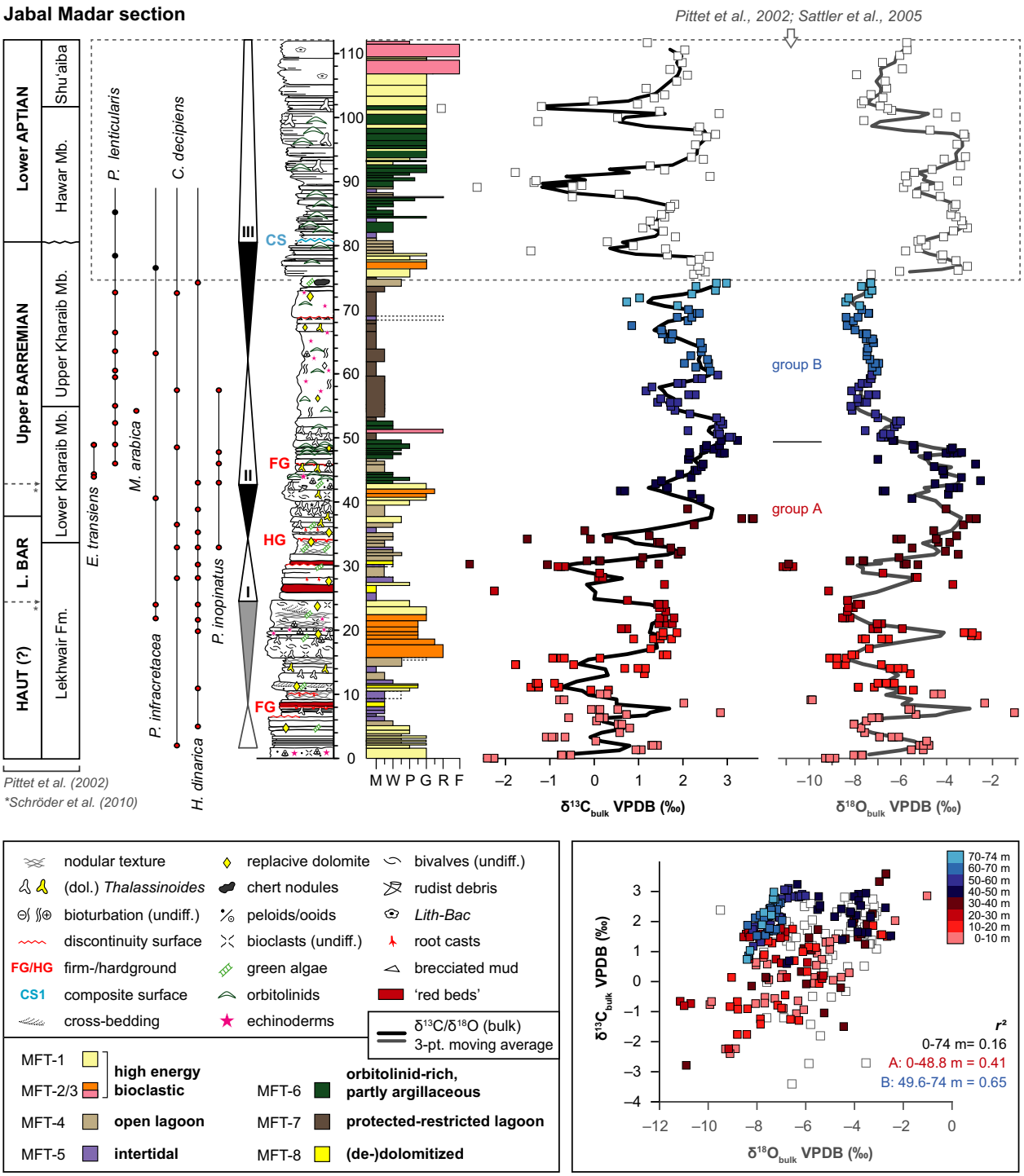

Fig. 4. Lithostratigraphy including identified microfacies types (MFT-1 to MFT-8) and main fossil constituents and carbon and oxygen isotope stratigraphy of the Jabal Madar section, complemented with data from Pittet *et al.* (2002) and Sattler *et al.* (2005). Sequence stratigraphic interpretation after Pittet *et al.* (2002). At first glance, the low covariance between $\delta^{13}C$ and $\delta^{18}O$ values (r^2 = 0·12) of all analysed bulk carbonate samples (0 to 74 m) points to the absence of major diagenetic alteration of isotope ratios. Splitting the data into two stratigraphic groups (A/B), however, provides r^2-values that are indicative of a moderate (0 to 48·8 m: r^2 = 0·41) to strong correlation (49·6 to 74 m: r^2 = 0·65) of carbon and oxygen isotope values.

Table 1. Principal carbonate microfacies types including biostratigraphically meaningful fossils based on thin section criteria (Jabal Madar section)

MFT	Facies	Samples	Key biota or aspects
1	Peloidal (bioclastic) pack-/grainstone	JM0.0, JM0.5, JM1.3, JM2, JM3.3, JM4.7, JM10.6, JM22.9, JM24, JM27.1, JM40.5, JM41.7, JM42.2, JM42.8	Often very fine grained and densely packed, various bioclasts: for example, benthic foraminifers (e.g. miliolids, *Praechrysalidina infracretacea*), dasycladacean algae (including *Coptocampylodon lineolatus* and calcitic *Hensonella dinarica*), rare rudist fragments
2	Intraclastic mollusc grain-/rudstone	JM16.1, JM18.6	Large well-rounded mollusc shells (incl. rudists) & intraclasts, faecal pellets, benthic foraminifers, peloids and dasycladacean algae
	Faecal pellet-mollusc packstone/ grainstone	JM19.1, JM19.6, JM21, JM21.9, JM41.2	Peloidal 'matrix', w-clasts, large faecal pellets, micritized and partly silicified mollusc shell fragments, benthic foraminifers, *H. dinarica*
3	Bacinelloid rudstone	JM51.1	Bacinelloid nodules in micritic to micropeloidal matrix, large faecal pellets, orbitolinids, echinoderm debris, altered rudist fragments
4	Open lagoonal biodiverse mudstone/wackestone	JM36.4, JM38.9, JM43.3, JM45.5, JM45.9, JM46.6, JM47.2, JM74	Varying abundance of echinoderms (syntaxial cements), calcareous algae (*Permocalculus inopinatus*, *H. dinarica*), fine sparitic mollusc debris, foraminifers (e.g. *Choffatella decipiens*) and small (often micritized) bioclasts, rare small oyster & rudist fragments, bioclastic-faecal pellet grainstone burrows
5	Intertidal restricted mudstone/wackestone	JM6.3, JM7.1, JM7.6, JM10, JM11.7, JM14, JM28.2, JM30.2, JM32.8, JM35.5, JM68.8	Often laminated or clotted peloidal texture, intercalated thin monospecies levels (e.g. ostracods, gastropods, sponge spicules, *H. dinarica*), sparite-filled root casts, mud brecciation, mud cracks
6	Orbitolinid-echinoderm wackestone/packstone	JM43.8, JM44.3, JM47.7, JM48.2, JM48.4, JM49.6, JM52.1, JM52.6	Abundant/dominant low-conical orbitolinids, common echinoderm debris, dark elongated mudstone clasts, faecal pellets, peloids, benthic foraminifers, sparitic shell debris (gastropods?), rare *H. dinarica*, partly argillaceous
7	Protected lagoonal echinoderm-orbitolinid mudstone/wackestone	JM53.7, JM54.3, JM54.9, JM55.5, JM56.1, JM56.7, JM57.3, JM59.2, JM60.4, JM63.4, JM65.4	Fine-grained echinoderm debris, rare to common orbitolinids, very rare benthic foraminifers
	Protected to restricted echinoderm mudstone	JM50.6, JM53.1, JM59.8, JM61.6, JM65.4, JM66.2, JM67.5, JM71.8, JM72.4	Fine-grained sparse echinoderm debris, very rare contributions of additional allochems, low to strong intraparticle micro-porosity (dissolved dolomite rhombs and small bioclasts), partly argillaceous
8	Dedolomite	JM8.6, JM11.1, JM26.1, JM30.3	Microcrystalline euhedral porphyrotopic or anhedral calcified dedolomite, masking of primary texture

when compared to the upper part (38·9 to 74 m; mean: 2·2‰; SD: 0·6‰). The mean intra-sample $\delta^{13}C_{bulk}$ variability is in the order of 0·4‰ (SD: 0·6‰).

Considering 3-point running mean values, deposits of the lower part of the section (0 to 11 m) record a positive $\delta^{13}C_{bulk}$ excursion with an amplitude of about 2·4‰, which is followed by a prolonged second positive 2·1‰ carbon isotope excursion (11 to 30·3 m). The latter excursion is terminated by a negative $\delta^{13}C_{bulk}$ spike representing the lowest values of the carbon isotope record (−2·8‰). Background $\delta^{13}C_{bulk}$ values are in the order of about −0·5‰. Upsection, the carbon isotope curve exhibits a prominent stepwise change (30·3 to 37·4 m) towards a maximum carbon isotope value of 3·6‰ (37·4 m). The subsequent chemostratigraphic segment (37·4 to 74 m) is characterized by sinusoidal $\delta^{13}C_{bulk}$ changes (amplitude: 1·5‰), which oscillate around a background value of about 2·2‰.

Bulk carbonate oxygen isotope ($\delta^{18}O_{bulk}$) values range between −11·1‰ and −1·0‰ (mean: −6·5.‰; SD: 1·9‰). The mean intra-sample $\delta^{18}O_{bulk}$ variability is in the order of 0·6‰ (SD: 0·7‰). Strong $\delta^{18}O_{bulk}$ oscillations characterize the lower part of the oxygen isotope curve (0 to 30·3 m; mean −6·9‰; SD: 1·9‰), superimposed by a

moderate trend to lower values (30·3 m: −11·1‰). Upsection, the oxygen isotope curve exhibits a prominent positive trend (30·3 to 31·8 m) that reaches a first plateau (31·8 to 48·4 m; mean −4·1‰; SD: 1‰), and finally a negative change (48·4 to 53·7 m) reaching a second plateau (53·7 to 74 m; mean −7·6‰; SD: 0·4‰). The latter plateau is characterized by low-amplitude sinusoidal changes in $\delta^{18}O_{bulk}$.

Cross-plots of bulk carbonate carbon and oxygen isotope data (Fig. 4) reveal a low covariance if all data are considered (0 to 74 m: $r^2 = 0{\cdot}16$). Based on petrographic (change towards mud-dominated 'chalky' limestones) and stable isotope features (lowering of $\delta^{18}O_{bulk}$ background values), as observed in the upper part of the Jabal Madar section, two different stratigraphic groups of bulk carbonate samples (A/B) might be distinguished. Splitting the stable isotope data into these groups provides r^2-values that are indicative of a moderate (A: 0 to 48·8 m: $r^2 = 0{\cdot}41$) to strong correlation (B: 49·6 to 74 m: $r^2 = 0{\cdot}65$) of carbon and oxygen isotope values.

Component-specific carbon and oxygen isotope variability

Carbon and oxygen isotope results of component-specific carbonate phases (matrix micrite, dedolomite, sparry cement, bivalve shell material) of selected samples derived from the Jabal Madar section are plotted in Figs 5 and 6.

The majority of matrix micrite *sensu stricto* subsamples provide rather positive carbon (0·9‰ to 3·2‰, mean: 2·1‰) and oxygen isotope values (−7·8‰ to −0·8‰, mean: −5·2‰). Bivalve subsamples largely overlap the range of these matrix micrite values, with carbon isotope values between 1·3‰ and 2·9‰ (mean: 2·1‰) and oxygen isotope values between −7·5‰ and −3·9‰ (mean: −5·8‰). A limited number of matrix micrite samples ($n = 8$) show lowered $\delta^{13}C$ values (−1·5‰ to 0·7‰, mean: −0·3‰) along with less variable $\delta^{18}O$ values (−5·2‰ to −4·1‰, mean: −4·8‰).

Strongly dedolomitized subsamples (dedolomite 75 to 95%) provide carbon isotope values ranging between −5·5‰ and 0·9‰ (mean: −2·0‰) and oxygen isotope values ranging between −12·3‰ and −7·6‰ (mean: −9·7‰). In contrast, moderately to weakly dolomitized samples (dedolomite 5 to 40%) record considerably less negative $\delta^{13}C$ (−0·5‰ to 1·9‰, mean: 0·8‰) and $\delta^{18}O$ values (−8·2‰ to −4·4‰, mean: −6·5‰).

Sampled cement phases are represented by drusy calcitic sparite that either fills bioclastic voids and intergranular pore space (spA) or fractures and voids (spB). In general, the distinguished cement generations bear clearly different isotopic signatures. SpB samples provide the most positive $\delta^{13}C$ (2·6‰ to 4·0‰, mean: 3·3‰) and $\delta^{18}O$ values (−3·9‰ to −2·2‰, mean: −3·2‰) of all sampled carbonate phases. In contrast, spA samples record a significantly wider range of both carbon (mean: −0·1‰, SD: 2·3‰) and oxygen isotope values (mean: −9·6‰, SD: 1·7‰). A cross-plot of $\delta^{13}C$ and $\delta^{18}O$ values (Fig. 6) allows two different groups of spA cements (spA-1, spA-2) to be distinguished. While spA-1 cements are moderately to strongly depleted in ^{13}C (−5·7‰ to −0·4‰, mean: −2·7‰) and ^{18}O (−7·9‰ to −14·1‰, mean: −10·8‰), spA-2 cements provide positive $\delta^{13}C$ values (0·4‰ to 2·4‰, mean: 1·2‰) along with less variable $\delta^{18}O$ values (−9·9‰ to −7·5‰, mean: 8·9‰).

Due to the often small size of cement-filled pore space, carbon (mean: 1·8‰, SD: 0·7‰) and oxygen isotope results (mean: −5·8‰, SD: 0·9‰) of a relatively large number ($n = 25$) of cement subsamples were discarded from further interpretations as they presumably represent a mixture of isotopic end-member compositions of spA and spB (Figs 5 and 6, see also Table SI-2), as will be further discussed.

Cathode luminescence characteristics, elemental geochemistry and strontium isotope analysis

The objective of CL microscopy (Fig. 7A–F) combined with elemental geochemistry and strontium isotope analysis (Fig. 7G) is to provide independent evidence for the stable isotope-based interpretation of diagenetic realms, in which certain carbonate phases were formed. If combined with a (semi-)quantitative assessment of identified diagenetic products (i.e. dedolomite, sparite cements) at thin section scale, this approach allows the impact of the latter on the stable isotope signature of mud-supported and grain-supported bulk carbonate material to be evaluated. Component-specific elemental concentrations (Mg, Sr, Fe, Mn: normalized to a calcium content of 39·7% for stoichiometric calcite), element/calcium and strontium isotope ratios are shown in Table 2. Only the most significant differences and similarities of analysed carbonate phases are reported here.

Cathode luminescence microscopy of matrix micrite reveals a commonly dull to moderately bright luminescence (Fig. 7A, B, and E). Dedolomite, often in the form of dedolomite rhombs, has a bright orange luminescence, contrasting with the duller surrounding matrix (Fig. 7C). SpA cements luminesce moderately to very bright orange to yellow and are characterized by a strongly zonal pattern (Fig. 7A and B). SpB cements mainly inhabit fractures that clearly truncate grains and previous spA cements (Fig. 7D) and reveal a luminescence ranging from predominantly dull to moderately bright orange. In contrast to spA, spB cements are far less subjected to

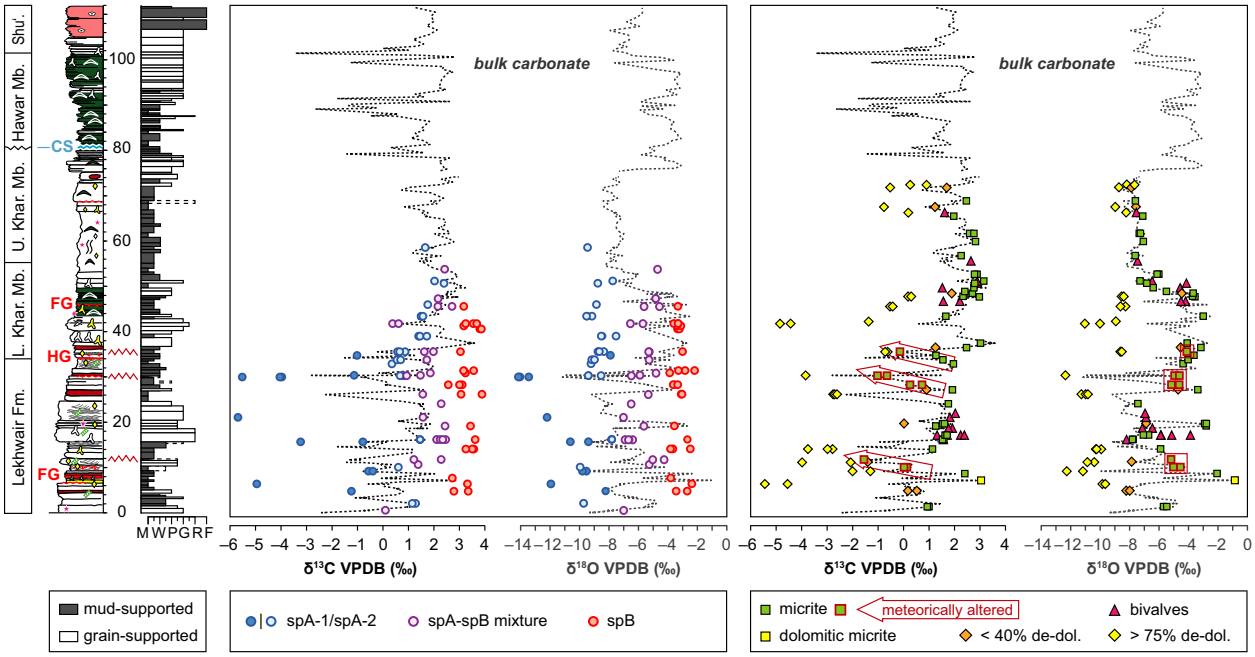

Fig. 5. Stratigraphic evolution of component-specific (sparite cements spA-1/2 and spB, calcitic/dolomitic micrite, low-Mg calcite bivalves, dedolomitized limestone) versus bulk carbonate carbon and oxygen isotope ratios (stippled line). Note the clearly different and rather uniform stable isotope signature of spB cements and the stratigraphic limited occurrence of matrix micrite samples recording meteorically induced negative carbon isotope changes. The component-specific approach reveals that the noisy carbon isotope pattern of bulk samples representing group A (0 to 48·8 m) is mainly caused by variable contributions of sparite cements and dedolomite. Please refer to the legend of Fig. 4 for information on symbols used in the rock column.

zoning. Both spA and spB cements frequently display partial alteration, expressed under CL by subordinate contributions of non-luminescent calcite and neomorphic microspar (Fig. 7B and E) or by intra-crystalline micropores producing a spotted bright orange luminescence pattern (Fig. 7A and D). Depending on the degree of recrystallization, bivalve fragments show a dull to dark luminescence (Fig. 7F).

Mudstone (matrix micrite) and grainstone (bulk) samples provide a wide range of elemental contents, but micrite values are considerably more variable (e.g. Fe(micrite): 27 to 962 p.p.m. vs. Fe (bulk): 136 to 465 p.p.m.). Notably, a cluster of matrix micrite samples showing largely invariant $\delta^{18}O$ values provide enhanced Fe/Ca ratios. Moreover, elemental and stable isotope analyses reveal that one matrix micrite sample (JM7.1D) is in fact composed of (early) dolomite (Ca/Mg: 2). In comparison with all other carbonate phases, the latter sample provides considerably enhanced (Mn/Ca)/(Sr/Ca) ratios and $\delta^{18}O$ and $\delta^{13}C$ values. Matrix micrite $\delta^{18}O$ values, plotted against (Mn/Ca)/(Sr/Ca) ratios, reveal a low correlation ($r^2 = 0{\cdot}2$). Strontium isotope ratios of a limited number of matrix micrite samples ($n = 4$) range from 0·707923 to 0·708947 (SD: $\pm 5/6 \times 10^{-6}$) and show a strong inverse correlation both with Sr/Ca ratios and $\delta^{18}O$ values. In

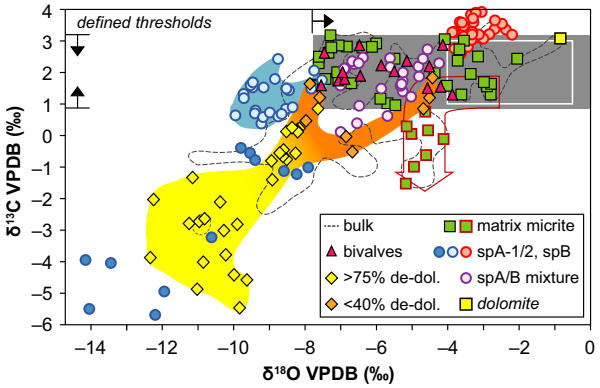

Fig. 6. Cross-plot of carbon and oxygen isotope ratios showing characteristic end-member compositions of identified carbonate phases (spA-2, spB, dolomitic micrite) and a clear covariant negative trend associated with variable contributions of dedolomite and spA-1 cements. Note an isotopic cluster representing the mixing of spA and spB signatures and a small cluster of micrite samples plotting along the meteoric calcite line of Lohmann (1988). The white rectangle marks the range of $\delta^{13}C$ and $\delta^{18}O$ values for Barremian open marine sea water (Jenkyns, 1995; Weissert & Erba, 2004; Godet *et al.*, 2006; Sprovieri *et al.*, 2006; Prokoph *et al.*, 2008; Bodin *et al.*, 2009; Wohlwend *et al.*, 2017). Here, established threshold values both for $\delta^{13}C$ and $\delta^{18}O$ are indicated by red triangles. The grey shaded area marks the range of 'filtered' bulk carbonate stable isotope signatures used for chemostratigraphic and palaeoenvironmental interpretations.

contrast, the best-preserved bivalve sample, JM46.6B, provides a considerably less radiogenic strontium isotope ratio (0·707556) along with enhanced strontium (710 p.p.m.) and very low iron (9 p.p.m.) and manganese (6 p.p.m.) contents.

Identified sparite cements (spA-1, spA-2, spB) show different elemental characteristics: mean magnesium and iron contents of spA-2 (Mg: 3385 p.p.m.; Fe: 370 p.p.m.) are enriched with respect to spB (Mg: 2525 p.p.m.; Fe: 14 p.p.m.), while the average strontium content of spA-2 (185 p.p.m.) is lower than those of spB (312 p.p.m.). Similar to matrix micrite and grainstone (bulk) samples, elemental contents of strongly dedolomitized limestone subsamples are highly variable (Table 1). Notably, sample JM11.1-DD provides similar elemental (high (Mn/Ca)/(Sr/Ca) ratios) and stable isotope properties (low $\delta^{18}O$ and $\delta^{13}C$ values) to spA-1 sample JM29.9.

DISCUSSION

Reliability of Jabal Madar bulk carbonate carbon and oxygen isotope data

At first glance, the Jabal Madar section exhibits a rather well-expressed bulk carbonate carbon isotope pattern (Fig. 4) that seems to allow for chemostratigraphic correlation purposes. Moreover, the low covariance between $\delta^{13}C$ and $\delta^{18}O$ values ($r^2 = 0{\cdot}16$) of all bulk carbonate samples points to the absence of major diagenetic alteration of isotope ratios. This prediction is obviously too simplistic, as the $\delta^{13}C_{bulk}$ and $\delta^{18}O_{bulk}$ cross-plot displays two different groups, each showing covariation between these proxies (Fig. 3). These groups comprise samples derived from the lower mixed mud-supported to grain-supported portion (0 to 48·8 m: group A, $r^2 = 0{\cdot}41$) and the whitish-weathering predominantly mud-supported upper portion (49·6 to 74 m: group B, $r^2 = 0{\cdot}65$) of the studied section. The observed difference of groups A and B is most likely related to primary contrasts in depositional setting (restricted vs. open lagoon; Pittet *et al.*, 2002) resulting in a variable sedimentary contribution from marine and terrestrial sources, which ultimately promote textural differences such as the size, amount and distribution of initially available pore space (among others). These in turn influence hydraulic conductivity, accounting for differential susceptibility to early and/or later diagenetic processes. As for the covariant trends depicted for bulk samples (groups A and B), two lines of reasoning can be brought forward: (i) the geochemical record was severely affected by mixing-zone diagenesis and obtained results no longer reflect original palaeoenvironmental conditions; (ii) sampling different generations of carbonate materials (matrix micrite, cements, dedolomite) may also produce such covariation, by which the original signal is still recorded at least in some carbonate phases (Allan & Matthews, 1982). In either case, differential diagenetic pathways must be explored in order to provide a clear understanding of the obtained bulk carbon and oxygen isotope patterns and determine if further interpretations based on the stratigraphic evolution of $\delta^{13}C_{BULK}$ should be pursued. In particular, the occurrence of dedolomite and sparite cement phases requires an in-depth evaluation as to their relative contribution to the bulk carbonate stable isotope archive. By means of a component-specific petrographic, elemental and stable isotope analysis, quantitative arguments can be used to extract an objectively reliable near-primary (shallow marine) carbon isotope signal which will allow a refined integrated stratigraphic framework to be established.

Component-specific geochemical and petrographic properties

It is widely accepted and demonstrated that $\delta^{13}C$ records are generally less affected by diagenetic overprint than the more sensitive $\delta^{18}O$ signal, as carbon isotopes are less vulnerable to changes in the water-rock ratio and suffer only minor alteration towards lower $\delta^{13}C$ values with increasing burial depth and associated increasing temperatures (Emrich *et al.*, 1970; Marshall, 1992). Diagenesis is thus often conservative when carbon isotopes are concerned, from sustaining absolute original values, to at least preserving the original trends along a studied time frame (Frank & Lohmann, 1996). In both cases, $\delta^{13}C$ records reflect original fluctuations in response to palaeoenvironmental conditions. Here, well preserved bulk carbon isotope signals were identified by focusing on the geochemical and petrographic properties of component-specific diagenetic products and eliminating their potential contribution to the obtained bulk $\delta^{13}C$ curve.

Both a stratigraphic and a cross-plot of carbon and oxygen isotope values illustrate the high variability in component-specific stable isotope signatures (Fig. 6). Although the elemental and isotopic composition of biogenic hard parts (Immenhauser *et al.*, 2008; Schöne, 2008) are known to severely depend on metabolic processes, previous studies have shown that bivalve shells might act as a suitable archive for mid-Cretaceous secular carbon isotope changes (Huck *et al.*, 2012; Huck & Heimhofer, 2015). Unfortunately, the petrographic inspection of bivalve shell fragments derived from the Jabal Madar section provides clear evidence for a moderate recrystallization and partial silicification of the fibrous low-Mg calcite ultrastructure. The majority of bivalve and matrix micrite carbon isotope values, in contrast to the highly variable bulk carbonate values, are close to the

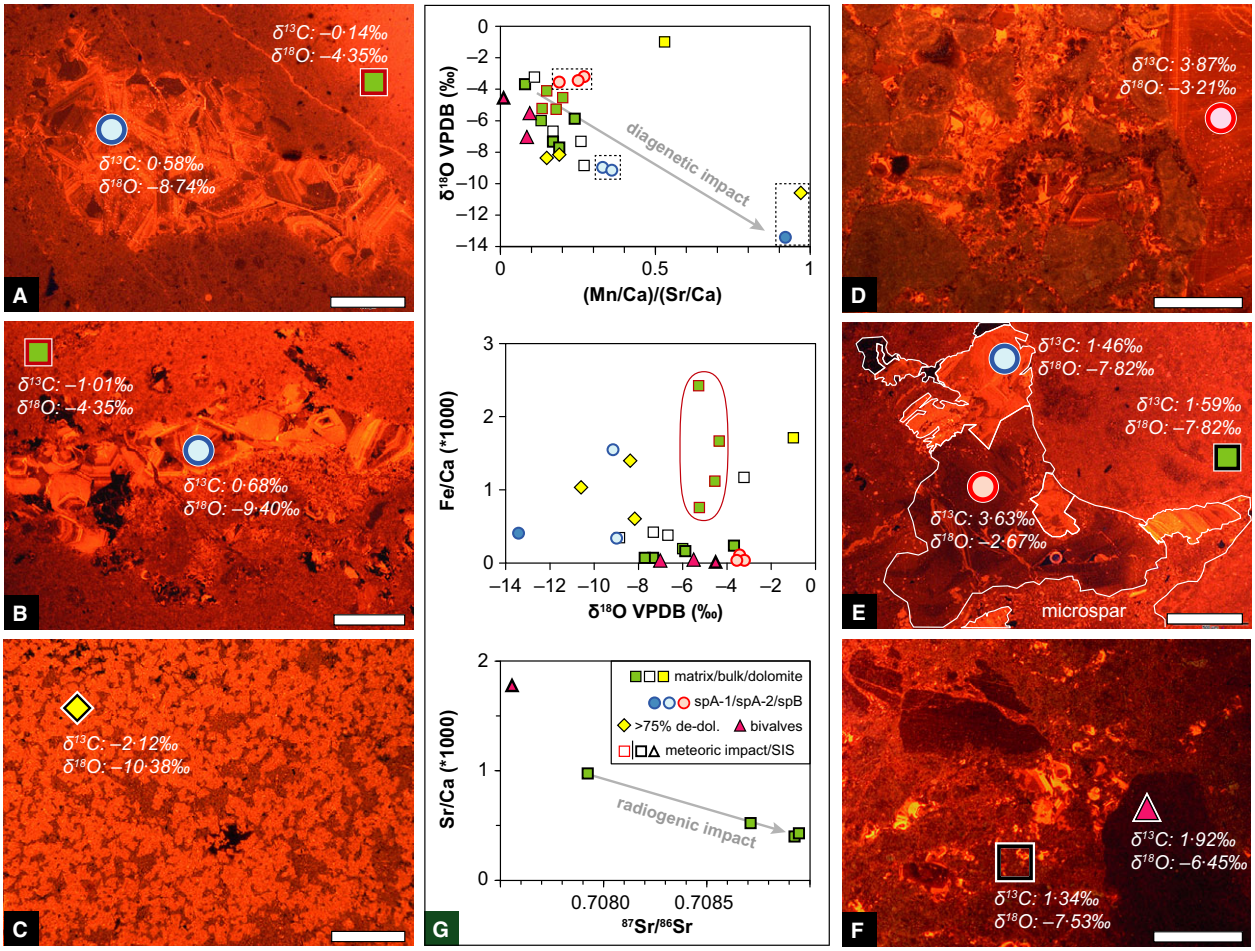

Fig. 7. Cathodoluminescence microphotographs (scale: 0·5 mm) and selected geochemical results of carbonate phases identified in samples derived from the Jabal Madar section. (A, B) Void-filling spA-2 cements showing a zoned cathodoluminescence pattern indicative of cement formation during a shallow to intermediate burial stage. SpA-2 voids are surrounded by a dull to slightly bright luminescing matrix with isotopic evidence for meteoric alteration. Partial alteration of spA-2 cement (B) is represented by dark (sparite) and blotchy (microsparite) patches. Samples JM35.5 and JM30.2. (C) Abundant replacive microcrystalline dedolomite rhombs characterized by a bright luminescence. Sample JM11.1. (D) Interfingering of spA-2 and spB cements, the former showing evidence for diminution by blotchy microsparite and dark luminescing calcite. Sample JM16.1. (E) Grainstone with dull to dark luminescing bivalve fragments and minor contribution of zoned intergranular spA-2 cement. (G) Cross-plots of selected component-specific geochemical proxies. SpA-1 cements and strongly dolomitized limestones showing the lowest oxygen isotope ratios provide the highest (Mn/Ca)/(Sr/Ca) values, thus indicating a diagenetic overprint (grey arrow) by similar fluids. Bivalves provide both the lowest (Mn/Ca)/(Sr/Ca) values and Fe/Ca ratios of all analysed subsamples, in contrast to a cluster of (arguably) meteorically altered matrix micrite providing considerably higher Fe/Ca ratios. A clear covariation in Sr/Ca ratios and strontium isotope ratios is observed among selected matrix micrite samples, an observation that points to the influence of radiogenic strontium related to siliciclastic weathering.

expected Barremian mean open marine $\delta^{13}C$ value of about 1 to 3‰ as recorded in Tethyan and Pacific pelagic sections (Weissert *et al.*, 1985; Jenkyns, 1995; Weissert & Erba, 2004; Godet *et al.*, 2006; Sprovieri *et al.*, 2006; Prokoph *et al.*, 2008; Bodin *et al.*, 2009; Wohlwend *et al.*, 2017). At first glance, this would imply that the most fine-grained portions of the Jabal Madar section escaped considerable overprint of their $\delta^{13}C$ signal by diagenetic fluids and thus, might be regarded as a suitable archive for secular carbon isotope trends of dissolved inorganic carbon (DIC). As stated by Immenhauser *et al.* (2008), however, neritic ooze 'cannot be considered to be free of diagenetic artefacts', as this polygenetic and therefore partly metastable material is expected to be prone to at least syn-depositional (pore-water) diagenesis (Patterson & Walter, 1994; Sanders, 2003; Walter *et al.*, 2007; Coimbra & Olóriz, 2012b). But such effects may result in only subtle changes to the original geochemical signals, thus even stabilized carbonates can provide reliable palaeoenvironmental records (Coimbra *et al.*, 2009; Vincent *et al.*,

Table 2. Analytical results (major and trace elements, strontium isotopes) of selected carbonate phases from the Jabal Madar section including bulk carbonate (grainstones), matrix micrite, sparite cements (spA-1, spA-2, spB) and strongly dedolomitized limestone

JM sample	$\delta^{13}C$	$\delta^{18}O$	Mg (p.p.m.)*	Sr (p.p.m.)*	Fe (p.p.m.)*	Mn (p.p.m.)*	Sr/Ca (×1000)	Fe/Ca (×1000)	Mn/Ca (×1000)	(Mn/Ca)/(Sr/Ca)	$^{87}Sr/^{86}Sr$
Grainstones											
0.0G	−2·25	−8·86	1186	158	136	44	0·40	0·34	0·11	0·27	
0.5G	−0·41	−7·94	1707	202	100	41	0·51	0·25	0·10	0·21	
11.7G	−0·95	−7·32	1955	285	166	75	0·72	0·42	0·19	0·26	
19.6G	1·86	−3·23	4121	308	465	35	0·78	1·17	0·09	0·11	
41.7G	0·69	−6·67	2335	242	151	42	0·61	0·38	0·11	0·17	
Matrix micrite											
7.1D	3·05	−0·84	114 100	164	391	87	0·72	0·98	0·38	0·53	
10M	0·14	−4·54	3587	466	444	94	1·17	1·12	0·24	0·20	
14M	1·14	−5·88	2032	207	64	50	0·52	0·16	0·13	0·24	0·708712
27.1M	1·93	−3·35	3791	387	93	31	0·97	0·24	0·08	0·08	0·707923
28.2M	0·27	−5·14	3444	289	962	51	0·68	2·30	0·12	0·18	
30.2M	−1·01	−4·94	2609	398	300	53	1·00	0·76	0·13	0·13	
35.5M	−0·14	−4·11	3865	532	662	78	1·27	1·60	0·19	0·15	
52.6M	2·89	−6·00	1997	200	77	26	0·50	0·19	0·07	0·13	
62.2M	2·56	−7·34	1127	159	27	27	0·40	0·07	0·07	0·17	0·708925
73.6M	2·30	−7·71	1173	170	28	33	0·43	0·07	0·08	0·19	0·708947
Dedolomite (>75%)											
11.1DD	−3·69	−10·59	2515	136	410	132	0·34	1·03	0·33	0·97	
47.7DD	0·28	−8·37	4339	395	555	57	0·99	1·40	0·14	0·15	
72.4DD	0·22	−8·17	1091	210	239	39	0·53	0·60	0·10	0·19	
Sparite A											
29.9SPA-1	−4·04	−13·42	1001	151	161	139	0·38	0·41	0·35	0·92	
33.7SPA-2	0·71	−8·98	3604	183	134	61	0·46	0·34	0·15	0·33	
43.3SPA-2	1·51	−9·15	3213	190	614	68	0·48	1·55	0·17	0·36	
Sparite B											
4.7SPB	2·79	−3·43	3265	242	43	61	0·61	0·11	0·15	0·25	
19.1SPB	3·45	−3·55	2363	366	14	68	0·92	0·04	0·17	0·19	
40.5SPB	3·87	−3·21	2721	293	14	80	0·74	0·04	0·20	0·27	
Bivalves											
17.1B	2·05	−5·51	2121	336	17	32	0·85	0·04	0·08	0·10	
18.6B	1·77	−7·03	1603	267	12	23	0·67	0·03	0·06	0·09	
46.6B	2·22	−4·51	1224	708	9	6	1·78	0·02	0·02	0·01	0·707556

*Normalized to a calcium content of 39·7% for stoichiometric calcite (except dolomitic micrite sample 7.1D).

2017). This possibility was tested by comparing carbon and oxygen isotope values, elemental contents and CL characteristics of matrix micrite (*sensu stricto*) with those of all other carbonate components identified in samples from the Jabal Madar section (Fig. 6), aiming to extract a highly detailed diagenetic evolution of the carbonate materials under study. Matrix micrite, in most of the thin sections, appears dull to moderately bright under CL. This often documented luminescence pattern mirrors the diagenetic stabilization of matrix micrite soon after deposition, either close to the sediment/water interface (Coimbra *et al.*, 2009) or in the shallow burial diagenetic domain. This interpretation is in line with the majority of matrix micrite $\delta^{13}C$ and $\delta^{18}O$ signatures, which are in the range of penecontemporaneous sea water isotope values (Coimbra *et al.*, 2009) or only slightly deviated towards (more negative) burial diagenetic signatures (Christ *et al.*, 2012).

Processes affecting carbon isotope signals

In line with sedimentological evidence for a restriction from the open marine realm and transient episodes of subaerial exposure (root traces, laminated mudstones with desiccation cracks or single-species (ostracod) assemblages), the stable isotope pattern ('inverted J") of a small cluster of bulk and matrix micrite samples ($n = 8$) documents the stratigraphically limited influence of mild meteoric diagenesis (Allan & Matthews, 1982; Meyers & Lohmann, 1985; Lohmann, 1988; Figs 5 and 6). The lack of a distinct and more profound exposure-related stable isotope pattern (strong decrease in $\delta^{13}C$ values related to

meteoric fluids bearing ^{12}C-enriched soil-gas CO_2) might be explained by (i) the initial palaeogeographic and climate setting, (ii) transient exposure periods inhibiting the formation of thick soil horizons, (iii) the erosion of the meteorically altered sediment pile during subsequent transgression and/or (iv) post-depositional dissolution–precipitation processes that might have masked the meteoric precursor signals (cf. Coimbra *et al.*, 2016; Godet *et al.*, 2016).

Subsamples with abundant microcrystalline replacive dedolomite (≥75%) as well as a cluster of sparite A subsamples (spA-1) provide the most negative carbon (and oxygen) isotope values. The impact of the latter diagenetic products on the bulk stable isotope composition is clearly related to their abundance, since samples with the lowest dedolomite contents (5 to 10%) record carbon (and oxygen) isotope values overlapping the isotope range of the best-preserved matrix micrite samples. This observation clearly reflects the mixing of the isotope signatures of the dedolomite end-member and the host rock, accounting for the fair correlation of both dedolomite subsamples and bulk samples of group A (Fig. 4; see also Table SI-3). Moreover, the observed (recent?) selective dissolution of replacive very small dedolomite crystals, although less abundant, appears to be associated with cyclic positive carbon isotope changes and thus results in rather strong correlation of isotope signatures of 'chalky' samples representing group B (Fig. 4). As carbon isotope values of dedolomite-rich samples are considerably depleted (down to −5·5‰), involved burial fluids might have been sourced by ^{12}C derived from the thermal breakdown of buried organic matter that escaped decomposition in the predominantly fine-grained portions of the Jabal Madar section. The alternative of early diagenetic meteoric fluids charged with soil-zone CO_2 that might have acted as donor of isotopically light carbon seems at first glance less likely. This alternative would imply the development of thick soil horizons and related mature karst features during a time (Late Barremian) of predominantly arid climate (Ruffell & Batten, 1990; Godet *et al.*, 2008; Föllmi, 2012; Amodio & Weissert, 2017). But even if erosion of former soil horizons occurred, the predicted oxygen isotope composition of meteoric waters in low latitudinal coastal settings contradicts this possibility (as further discussed).

Sparite A (spA) cements reveal two different carbon isotope signatures, from strongly to only slightly lowered values when compared to the range of presumed well-preserved marine signals. This feature reveals the influence of different sources of fault fluids, which may relate to multi-stage faulting events or merely to different directions of faulting (bed normal, parallel or oblique veins) promoting the circulation of different fluids (Agosta *et al.*, 2008). The least ^{13}C-depleted set of samples (spA-2) is characterized by a well-expressed zoned luminescence and low strontium contents (mean: 185 p.p.m.), and thus corresponds to shallow burial conditions, while the major departure from the expected marine $\delta^{18}O$ signal (Weissert *et al.*, 1985; Jenkyns, 1995; Weissert & Erba, 2004; Godet *et al.*, 2006; Sprovieri *et al.*, 2006; Prokoph *et al.*, 2008; Bodin *et al.*, 2009; Wohlwend *et al.*, 2017) recorded by spA-1 cements is at first glance consistent with deep burial fluids, as previously discussed.

Sparite B (spB) samples provide enigmatic, considerably higher carbon isotope signatures (up to 4‰) when compared to any other carbonate material and to the expected Barremian (shallow-) marine signal (Fig. 6). The timing of late veining and concomitant infill of available pore space of spB cements is hard to establish, but major spB veins cross-cut most of the remaining diagenetic features, so their origin is probably related to fluids circulating during or after sub-recent exhumation (and creation of secondary pore space due to dissolution processes) of the Cretaceous succession during the Miocene (Fig. 8). Due to similar carbon and oxygen isotope compositions of all spB cements and their encasing matrix micrite (not influenced by meteoric alteration), the influence of rock-buffered fluids is envisaged, but the clear increase in carbon isotope values merits attention (Fig. 5). The persistently higher carbon isotope signature is not abrupt enough to consider processes related to fermentation of organic acids, CO_2 reduction or excessive evaporation (Clayton, 1994). Alternatively, a slight carbon isotope fractionation is here proposed, owing to lowered pCO_2 in fluids circulating at shallow depth, which is reasonable during pressure release phenomena (Shemesh *et al.*, 1992; Hassan, 2011). Several reports of slightly heavier $\delta^{13}C$ values along late diagenetic calcite and even dolomite veins show a similar pattern (Morad *et al.*, 2010; Vandeginste *et al.*, 2013; Arndt *et al.*, 2014; Balsamo *et al.*, 2016). In any case, these cements are mostly well-expressed with respect to their textural (predominantly cross-cutting thick veins), CL (dull) and elemental characteristics (low Fe and Mn contents) (Figs 7 and 8). Bulk samples, in particular if mud-supported, are thus unlikely to be influenced by the geochemical signal of spB. As mentioned earlier, however, CL indicates that a limited number of cement-rich, grain-supported samples host interfingering sparite cements of spA and spB and/or provide evidence for sparite cement diminution by neomorphic microsparite patches (Fig. 7F). Carbon isotope values of the corresponding cements indeed reflect a mixture of spA and spB end-member compositions (Fig. 5). Consequently, the variable contribution of spB cements and microspar might shift the bulk carbon isotope signature towards higher values.

Processes affecting oxygen isotope signals

Regarding oxygen isotope values, the least depleted carbonate materials are matrix micrite, spB cements, selected bivalve shells and very weakly dedolomitized samples (Fig. 6). These partially overlap the expected marine signal, tailing towards the uppermost range of spA-2 cements. Selected bivalve shells showing partly preserved growth increments display rather low $\delta^{18}O$ values (−7·0 to −4·5‰) and strontium concentrations (336 to 708 p.p.m.), both geochemical signatures pointing to the alteration of shells in the shallow burial realm by marine fluids, despite their rather low iron (mean: 12 p.p.m.) and manganese (mean: 20 p.p.m.) concentrations. In line with considerably lowered $\delta^{18}O$ values of spA-2 cements, this confirms the progressive influence of fluids with elevated temperature in a rock-buffered system (Moore, 1985; Choquette & James, 1987; Allan & Wiggins, 1993; van der Kooij *et al.*, 2009), generating more depleted $\delta^{18}O$ values in carbonate phases precipitating from marine fluids in the intermediate burial realm.

Notably, a specific group of sparite cements (spA-1) and carbonates with a high abundance of dedolomite are strongly depleted in oxygen isotope values (down to −14‰), along with also very negative $\delta^{13}C$ values (down to −6‰). Perhaps the best explanation for the observed strongly depleted carbon and oxygen isotope values, as opposed to the thermal breakdown of buried organic matter in the deep burial realm, is the burial and subsequent expulsion of soil-zone CO_2-enriched meteoric waters (de Caritat & Baker, 1992; Moss & Tucker, 1995; Hendry, 2002; Frazer *et al.*, 2014). A precursor meteoric $\delta^{18}O$ signature of −5‰ would then translate into a maximal burial depth of 1·9 km, well within the range of a previously estimated intermediate burial depth of 1 to 4 km for Cretaceous deposits exposed along the Adam foothills at Jabal Madar and Jabal Qusaybah (Hanna, 1990; Mozafari *et al.*, 2015). This alternative is also favoured against the contribution of thick former soil horizons, because the recorded shift in oxygen isotope ratios of meteoric waters towards values of up to −14‰ is incompatible with the minimal effect of isotopic fractionation during evaporation – precipitation (Rayleigh Effect) at low latitudinal coastal settings (Dansgaard, 1964; Anderson & Arthur, 1983; Lohmann, 1988).

Establishing isotopic threshold signals

Although the contribution of burial-related diagenetic processes evidently influenced the oxygen isotope signature of Jebel Madar bulk carbonate, they are generally not believed to have a major impact on carbon isotope geochemistry (Banner & Hanson, 1990; Veizer *et al.*, 1999), in particular if cements are volumetrically of low importance. In fact, even bulk carbon isotope values recorded by cement-rich (spA-2) grain-supported samples largely resemble those of matrix micrite samples (1 to 3‰) and, more importantly, of selected best-preserved bivalve shells. However, the evaluation of component-specific isotope signatures (bulk vs. spA-2) revealed that enhanced spA-2 contents in the order of about 25% (sample JM40.5) result in a lowering of the $\delta^{13}C_{bulk}$ value by about 0·7‰ (Fig. 7D; Table SI-2). At limited stratigraphic intervals, this lowering of $\delta^{13}C_{bulk}$ values is counteracted by the partial replacement of spA-2 cements by a later diagenetic cement (spB) bearing considerably higher carbon (and oxygen) isotope values.

In order to provide solid evidence for the usefulness of bulk carbon isotope values and overall stratigraphic trends for further chemostratigraphic and palaeoenvironmental interpretations, critical thresholds established by the in-depth analysis of component-specific samples have to be applied. In particular, the stable isotope signatures of mud-supported, often dedolomite-rich (≥75%), and cement-rich grain-supported portions (group A) of the Jabal Madar section merit attention. These samples either experienced mild early meteoric diagenesis (10 to 12 m, 28 to 36 m; Fig. 5) or severe diagenetic alteration by buried meteoric waters during the mesogenetic stage (Fig. 5). It is therefore concluded that the variable contribution of dedolomite and sparite A largely dictates the diagenetic trends obtained for bulk carbonate samples. In order to confidently establish a carbon isotope threshold that is not affected by either of these cement phases, bulk stable isotope signatures overlapping with those provided by meteorically altered samples, strongly dedolomitized samples and spA-1 samples ($\delta^{18}O$ <−7·8‰, $\delta^{13}C$ <0·9‰) are discarded from further stratigraphic and palaeoenvironmental interpretations. Moreover, the possible influence of spB cements on the bulk carbonate record is lowered by excluding samples with $\delta^{13}C$ values above 3·1‰. Notably, the filtered bulk carbonate samples (107 out of 202 samples) fall within matrix micrite *sensu stricto* (not influenced by meteoric fluids) and selected bivalve shell isotope signals.

In summary, the in-depth component-specific petrographic and geochemical approach presented here allows the Jabal Madar shallow-water bulk carbonate carbon isotope archive to be critically assessed. The resulting 'cleaned' carbon isotope record is expected to have preserved a near-primary pattern of superimposed global $\delta^{13}C$ trends and inflexion points.

Integrated Barremian–Aptian shallow-water stratigraphy of Northern Oman

The Barremian–Lower Aptian portion of the Jabal Madar section shows a characteristic sedimentary stacking pattern, which is easily recognizable in the field as repeated

alternation of (i) predominantly thin bedded partly argillaceous (upper Lower Kharaib and Hawar members) and (ii) more massive and partly cross-bedded intervals (lower Lower Kharaib, Upper Kharaib and Lower Shu'aiba; Fig. 3A). The latter depositional cycles are well-documented throughout the Arabian platform both in outcrops and in the subsurface and referred to as third-order sequences I (AP Bar1), II (AP Bar2) and III (AP Apt1-4) (Harris *et al.*, 1984; Hughes-Clarke, 1988; Sharland *et al.*, 2001; Pittet *et al.*, 2002; van Buchem *et al.*, 2002; Strohmenger *et al.*, 2006; van Buchem *et al.*, 2010). Following a revised Barremian–Aptian orbitolinid biostratigraphic zonation of the eastern Arabian Plate (Schröder *et al.*, 2010), the occurrence of the short range index fossils *M. arabica* (see also Simmons, 1994) and *E. transiens* in the transgressive deposits of the upper Lower Kharaib Member at Jabal Madar (sequence II) is indicative of an early to middle Late Barremian age, whereas the mass occurrence of *P. lenticularis* in the early transgressive Hawar Member points to an early Early Aptian age.

The 'filtered' bulk carbonate carbon isotope stratigraphic record established here (complemented with data from Sattler *et al.*, 2005) allows for a chemostratigraphic characterization of the combined biostratigraphic-sequence stratigraphic scheme (Pittet *et al.*, 2002; Schröder *et al.*, 2010). Initially, carbon isotope stratigraphy is applied to correlate sequences I to III on a regional (Oman) scale. Unfortunately, continuous Barremian–Aptian shallow-water carbon isotope records are scarce throughout the Arabian platform. Two exceptions are the uppermost Barremian–Lower Aptian Wadi Mu'aydin $\delta^{13}C$ record from the southern rim of the Jebel Akhdar dome in northern Oman (Wilson, 1969; Glennie *et al.*, 1974; Simmons & Hart, 1987; Simmons, 1990; van Buchem *et al.*, 2002) and the Upper Barremian–Lower Aptian Huqf $\delta^{13}C$ record (section S018) from south-eastern Oman (Immenhauser *et al.*, 2004; Sattler *et al.*, 2005).

In the Huqf area (Fig. 9), partly dolomitized tidal flat deposits representing the highstand of sequence I display lowered and strongly fluctuating carbon isotope values. This pattern has been associated with local water mass 'ageing' and superimposed repeated subaerial exposure events in the intertidal realm (Sattler *et al.*, 2005). In the relatively more distal Jabal Madar section, a limited number of matrix micrite subsamples within transgressive and early highstand deposits of sequence I also record meteorically induced negative carbon isotope changes in the order of up to 3‰. The arguable meteoric origin of these negative $\delta^{13}C$ excursions is supported by enhanced iron (mean: 641 p.p.m.) contents recorded by micrite samples and the occurrence of delicate spar-filled root casts and thin laminated mudstone layers (Table 2; Figs 7 and 9).

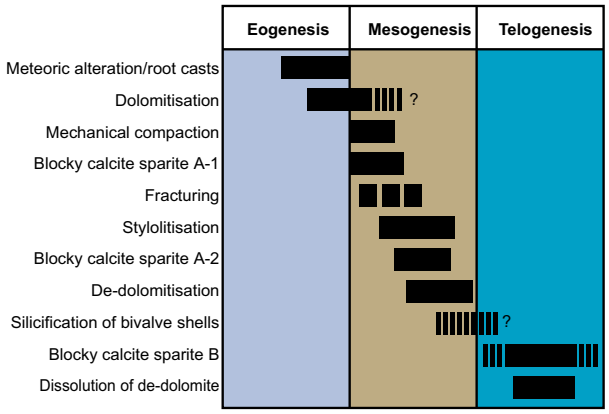

Fig. 8. Paragenetic sequence of different diagenetic processes and products as recorded by Barremian–Aptian shallow-water limestones at the Jabal Madar dome.

The overlying largely grain-supported high-energy deposits representing the late highstand of sequence I, in contrast, lack clear isotopic and petrographic evidence for a substantial overprint by meteoric fluids. Considering CL characteristics (showing dominance of spA-2 cements), this might be explained by burial-related dissolution–precipitation processes.

Chemostratigraphically, sequence II both at Jabal Madar and Huqf is represented by cyclic carbon isotope fluctuations superimposed on a broad positive $\delta^{13}C$ bulge. At all considered localities including Wadi Mu'aydin, sequence II is terminated by a prominent negative incursion immediately beneath the onset of the overlying *Palorbitolina lenticularis*-rich Hawar Member. At Jabal Madar and Huqf, this change is associated with laterally extensive composite surfaces (CS) that bear evidence for both a subaerial exposure and a marine hardground stage (Sattler *et al.*, 2005). This observation supports the notion of a major sea-level fall and subsequent long-lasting exposure (10^5 years) of the Arabian carbonate platform at the Barremian–Aptian transition (van Buchem *et al.*, 2002; Al-Husseini & Matthews, 2010).

At Jabal Madar and Wadi Mu'aydin, the transgressive deposits of sequence III record gradually increasing carbon isotope values (Hawar Member), which are again capped by an abrupt negative 2‰ change in $\delta^{13}C$ at the transition towards the *Lithocodium–Bacinella* bearing deposits of the Lower Shu'aiba Member. Following previous work in Oman (van Buchem *et al.*, 2002; Sattler *et al.*, 2005; Huck *et al.*, 2010), the observed prominent negative $\delta^{13}C$ spike represents the chemostratigraphic segment C3 *sensu* Menegatti *et al.* (1998), which precedes oceanic anoxic event (OAE) 1a. The Huqf section provides a rather similar pattern, but due to the restricted intertidal conditions, $\delta^{13}C$ values of the Hawar Member

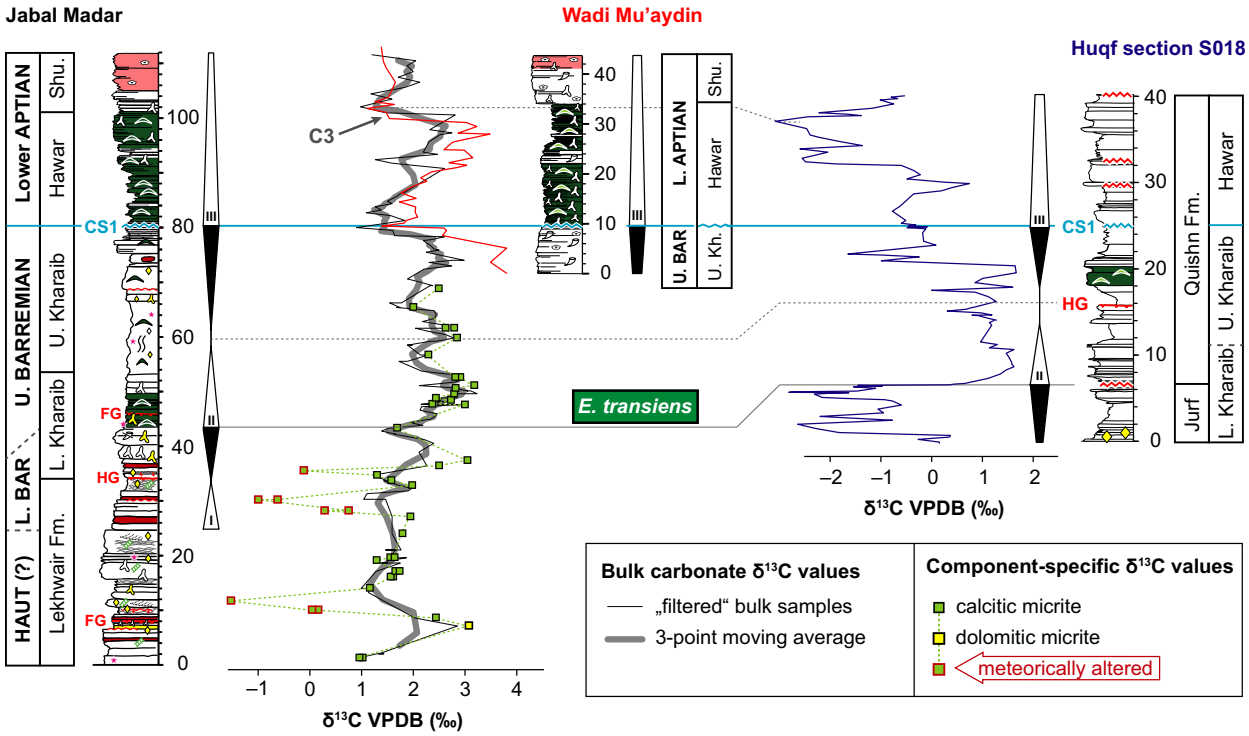

Fig. 9. Chemostratigraphic characterization of the combined biostratigraphic-sequence stratigraphic scheme established for Arabian carbonate platform sections (Jabal Madar, Wadi Mu'aydin, Huqf S018) in Oman (van Buchem *et al.*, 2002; Pittet *et al.*, 2002; Sattler *et al.*, 2005; Schröder *et al.*, 2010). Note that bulk carbonate stable isotope results of Jabal Madar samples (including data from Sattler *et al.*, 2005) have been filtered following the threshold values established here for $\delta^{13}C$ (>0·9‰, <3·1‰) and $\delta^{18}O$ (>−7·8‰). The thick grey line represents the 3-point moving average curve. Matrix micrite carbon isotope values (stippled green line) largely resemble those of 'filtered' bulk carbonate samples (thin black line). Exceptions are (i) a single dolomitic sample showing elevated carbon and oxygen isotope values and (ii) a few micrite samples recording lowered $\delta^{13}C$ values along with invariant $\delta^{18}O$ values, indicating the impact of meteoric diagenesis (and elevated Fe contents: Table 2). Please refer to the legend of Fig. 4 for information on symbols used in the rock column.

are strongly overprinted by meteoric carbon isotope signatures (Sattler *et al.*, 2005).

In contrast to the rather well-established, integrated stratigraphic framework for the Upper Barremian–Lower Aptian carbonate platform deposits exposed at Jabal Madar, Wadi Mu'aydin and the Huqf area, the long range of the Hauterivian-Early Barremian *Permocalculus inopinatus* biozone (Simmons, 1994) hampers a precise carbon isotope-based age assignment for the Upper Lekhwair Formation and Lower Kharaib Member at Jebel Madar, in particular, as additional carbon isotope stratigraphic results from Wadi Mu'aydin and the Huqf area are presently not available.

Since the petrographic and geochemical properties of certain carbonate phases clearly indicate a rather complex multi-stage diagenetic alteration of the considered interval at Jabal Madar (Fig. 8), the aim is to establish a best-fit chemostratigraphic framework by considering Tethyan-wide neritic and pelagic major carbon isotope and biosedimentation changes (Fig. 10). The Northern Tethyan Cluses section serves as a chemostratigraphic shallow-water reference, as the Barremian–Aptian carbon and strontium isotope pattern recorded at this locality allowed precise correlation with well-dated pelagic sections (Angles, Gorgo a Cerbara) in the Vocontian and Umbria Marche basins (Busnardo, 1965; Godet *et al.*, 2006; Sprovieri *et al.*, 2006; Bodin *et al.*, 2009; Huck *et al.*, 2011, 2013; Stein *et al.*, 2011). An age-calibrated carbon and strontium isotope reference frame (Huck & Heimhofer, 2015) builds on this platform-to-basin correlation, providing a well-constrained Barremian pattern with distinct chemostratigraphic tie points including (i) a positive change in pelagic $\delta^{13}C$ background values known as the Mid-Barremian Event (MBE), (ii) a Late Barremian gradual (pelagic) positive carbon isotope bulge, and (iii) the above-mentioned negative variation in $\delta^{13}C$ at the Barremian–Aptian boundary.

The MBE has been arguably associated with a relative increase in the basinward export of platform-derived aragonitic detritus (Föllmi *et al.*, 2006; Godet *et al.*,

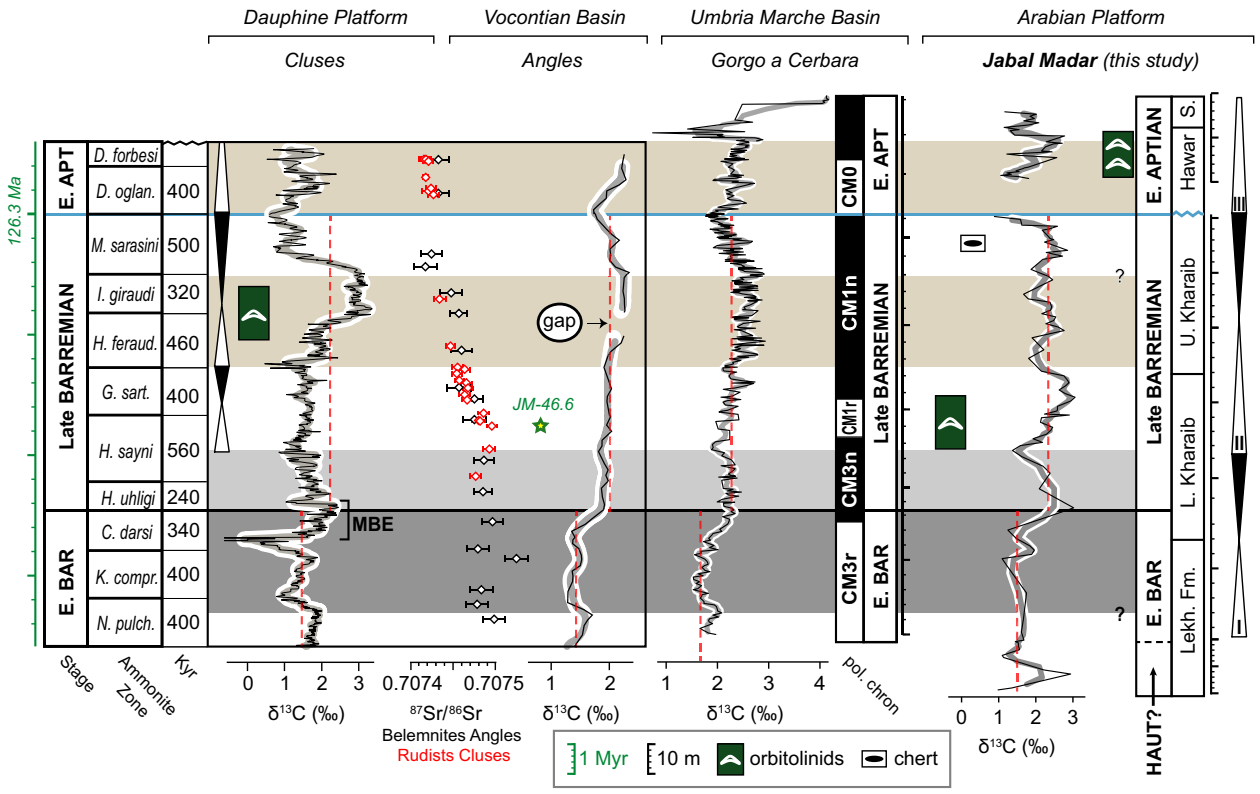

Fig. 10. Carbon isotope based correlation of the 'filtered' Jabal Madar record with age-calibrated neritic (Cluses) and basinal (Angles, Gorgo a Cerbara) reference records (Godet *et al.*, 2006; Sprovieri *et al.*, 2006; Huck *et al.*, 2011; Stein *et al.*, 2011; Huck & Heimhofer, 2015). Note extremely low Barremian carbonate preservation rates as calculated from the Jabal Madar section. Thick grey lines represent 3-point moving average curves. Dashed red lines highlight a positive shift in pelagic (and arguably neritic) $\delta^{13}C$ background levels at the onset of the Late Barremian. The stratigraphic position of major discontinuity surfaces (CS) and orbitolinid-rich levels are indicated.

2006) in the Northern Tethyan realm, although sedimentological evidence seems to promote enhanced black-shale formation in the Boreal (Lower Saxony Basin: Malkoč & Mutterlose, 2010) and central Tethyan realms (Umbria Marche Basin: Sprovieri *et al.*, 2006) as a potential driver of this change in pelagic carbon isotope values. In shallow-water sections, the MBE is generally less well-constrained due to the overall large variability in $\delta^{13}C$, which is in particular related to the exposure-related meteoric overprint of deposits in the prelude and aftermath of the MBE (Di Lucia *et al.*, 2012; Huck *et al.*, 2013). At all considered reference sections, however, the chemostratigraphic pattern beneath the MBE-positive values is characterized by a two-fold negative $\delta^{13}C$ excursion, the latter linked to a major subaerial exposure event in the Northern Tethyan realm (Huck *et al.*, 2013). Notably, a similar pattern of transient (meteorically induced) negative values and a subsequent prominent positive excursion in $\delta^{13}C$ is recorded at Jabal Madar (30 to 38 m; Fig. 9).

The onset of the gradual positive carbon isotope bulge in the Umbria Marche Basin coincides with the onset of rhythmic black-shale deposition (Sprovieri *et al.*, 2006). At Cluses, this positive trend appears to be attenuated by local carbon cycling processes that shift the carbon isotope record towards more negative values. There, a return to more open marine conditions is documented by a rapid and prominent $\delta^{13}C$ shift within transgressive *Palorbitolina lenticularis*-rich deposits ascribed to the *Hemihoplites feraudianus* ammonite zone. Due to the influence of platform-derived carbonate detritus, the adjacent hemipelagic Angles section in the Vocontian provides a similar carbon isotope pattern (Föllmi *et al.*, 2006). The stepwise positive carbon isotope trend as displayed by the shallow-water Jabal Madar record shares similarities with the Umbria Marche $\delta^{13}C$ pattern. In contrast to the Cluses section, slightly argillaceous *Palorbitolina*-rich deposits occur at Jabal Madar already at the onset of the positive carbon isotope bulge (*~Heinzia Sayni* ammonite zone). An oyster fragment derived from this interval at Jabal Madar provided a strontium isotope value (0·707556) that slightly deviates from the expected range of $^{87}Sr/^{86}Sr$ values (0·707450 to 0·707500) for Barremian sea water (McArthur *et al.*, 2001; Huck *et al.*,

2011). Given the observed increased shedding of clay in the upper Lower Kharaib Member at Jabal Madar, as well as the clear radiogenic strontium isotope signature as recorded by matrix micrite samples (0·707923 to 0·708947, Fig. 7), the observed shift towards more positive values is interpreted to reflect the influence of riverine input of radiogenic strontium related to continental silicate weathering. In accordance with previous SIS studies based on oyster shells in Cretaceous coastal settings (Burla *et al.*, 2009; Heimhofer *et al.*, 2012; Horikx *et al.*, 2014), a moderate radiogenic impact on the $^{87}Sr/^{86}Sr$ signature (*ca* 5×10^{-6}) of the best-preserved shell selected here is assumed. The measured value might therefore support an early Late Barremian age. Without additional strontium isotope samples that might record secular trends of radiogenically influenced shallow marine $^{87}Sr/^{86}Sr$, however, this age assignment remains tentative.

In summary, the integration of sequence stratigraphic and biostratigraphic data (Pittet *et al.*, 2002 and this study) with the evaluated bulk carbonate $\delta^{13}C$ record enables a chemostratigraphic characterization of the Jabal Madar section. Considering this integrated stratigraphic framework, the diachronous nature of Late Barremian orbitolinid mass occurrences as recorded by northern and southern Tethyan transgressive carbonate platform deposits becomes evident. However, a precise chemostratigraphic age assignment of Hauterivian to Lower Barremian shallow-water carbonates of the Arabian carbonate platform is still problematic due to (i) the low-resolution of shallow-water biostratigraphic zonation schemes and (ii) the lack of carbon isotope records along the Arabian carbonate platform, which hamper distinguishing between local (diagenetic) and global carbon isotope perturbations and the identification of carbon isotope gradients across the platform. Moreover, extremely reduced Barremian carbonate preservation rates (*ca* 0·012 mm y^{-1}) reveal that large parts of the carbon isotope signal at the Jabal Madar locality is lost in discontinuity surfaces. The platform-wide assessment of component-specific carbon isotope records, however, has the potential to solve these stratigraphic uncertainties, in particular if combined with SIS, which focuses on secular rather than short-term changes in marine $^{87}Sr/^{86}Sr$.

CONCLUSIONS

- Bulk carbonate stable isotope signatures recorded by a tropical mid-Cretaceous (Barremian–Aptian) shallow-water limestone succession (Jabal Madar section, Oman) provide evidence for a differential multi-stage diagenetic alteration. This is revealed by two stratigraphic clusters of samples providing significant correlations of carbon and oxygen isotopes.
- An in-depth petrographic (CL microscopy) and geochemical evaluation (C, O, Sr isotopes, trace elements) of different carbonate phases shows evidence for a stratigraphically variable and often facies-related impact of different diagenetic fluids on the bulk-rock stable isotope signature.
- The presence of abundant replacive dedolomite in mud-supported limestone samples forced negative carbon and oxygen isotope changes that are either associated with the thermal breakdown of organic matter in the deep burial realm or the expulsion of buried meteoric water in the intermediate burial realm.
- Sparite cements filling intergranular pores, bioclastic voids and fractures (spA) evidence intermediate to (arguably) deep burial diagenetic conditions during their formation, owing to different timing or differential faulting promoting the circulation of fluids from different sources. In contrast, a second group of sub-vertical vein-filling sparite cements (spB) reveal a rock-buffered diagenetic fluid composition with an intriguing slight enrichment in carbon isotope values, probably due to fractionation during pressure release in the context of the Miocene exhumation of the carbonate platform deposits under study.
- The superposition of stable isotope signatures of identified carbonate phases causes a complex and often noisy bulk carbon isotope pattern that offers multiple chemostratigraphic interpretations due to the low-resolution of biostratigraphic constraints. The component-specific isotopic and petrographic approach defined threshold values for $\delta^{13}C$ (>0·9‰, <3·2‰) and $\delta^{18}O$ (>−7·8‰) that allowed the diagenetically least altered samples to be extracted and thus identify the most reliable 'primary' bulk carbon isotope signatures.
- The integration of the 'filtered' carbon isotope curve with lithostratigraphic, sequence stratigraphic and biostratigraphic data allows the Jabal Madar section to be compared with two (regional) Upper Barremian–Lower Aptian shallow-water sections in Northern (Wadi Mu'aydin) and southern Oman (Huqf). Although extremely low carbonate preservation rates at all considered localities reveal that most of the carbon isotope signal is lost in discontinuity surfaces, characteristic long-term trends as observed in the Jabal Madar record allow for a (tentative) chemostratigraphic correlation with stratigraphically well-constrained Tethyan reference carbon isotope curves. Chemostratigraphic tie points include (i) a positive shift in pelagic and neritic background $\delta^{13}C$ values referred to as the Mid-Barremian Event, (ii) a long-lasting Late Barremian-positive

carbon isotope bulge and finally (iii) two distinct negative $\delta^{13}C$ values marking major palaeoceanographic changes at the Barremian–Aptian boundary and at the onset of the Early Aptian Oceanic Anoxic Event 1a.

ACKNOWLEDGEMENTS

We thank Christiane Wenske (LUH) for laboratory assistance and Katharina Müller (LUH) for thin section preparation. Financial support from SNF project IM44/2-1 is gratefully acknowledged. R. Coimbra is supported by the Post-Doctoral Fellowship SFRH/BPD/92376/2013 (Fundação para a Ciência e Tecnologia – FCT, Portugal) and the research units GeoBiotec-UID/GEO/04035/2013 and MARE-UID/MAR/04292/2013. The insightful comments by Alexis Godet and two anonymous reviewers are gratefully appreciated.

References

Agosta, F., Mulch, A., Chamberlain, P. and **Aydin, A.** (2008) Geochemical traces of CO_2-rich fluid flow along normal faults in central Italy. *Geophys. J. Int.*, **174**, 758–770.

Al-Husseini, M.I. and **Matthews, R.K.** (2010) Tuning Late Barremian – Aptian Arabian Plate and global sequences with orbital periods. In: *Barremian – Aptian Stratigraphy and Hydrocarbon Habitat of the Eastern Arabian Plate* (Eds van Buchem F.S.P., M.I. Al-Husseini, F. Maurer and H.J. Droste), *GeoArabia Spec. Publ.*, **4**, 199–228.

Allan, J.R. and **Matthews, R.K.** (1982) Isotope signatures associated with early meteoric diagenesis. *Sedimentology*, **29**, 797–817.

Allan, J.R. and **Wiggins, W.D.** (1993) Dolomite reservoirs: geochemical techniques for evaluating origin and distribution. *AAPG Cont. Educ. Course Notes Ser.*, **36**, 129.

Amodio, S. and **Weissert, H.** (2017) Palaeoenvironment and palaeoecology before and at the onset of Oceanic Anoxic Event (OAE)1a: reconstructions from Central Tethyan archives. *Palaeogeogr. Palaeoclimatol. Palaeoecol.*, **479**, 71–89.

Anderson, T.F. and **Arthur, M.A.** (1983) Stable isotope of oxygen and carbon and their application to sedimentologic and paleoenvironmental problems. *Soc. Econ. Palaeontol. Mineral. Short Course*, **10**, 1–151.

Arndt, M., Virgo, S., Cox, S.F. and **Urai, J.L.** (2014) Changes in fluid pathways in a calcite vein mesh (Natih Formation, Oman Mountains): insights from stable isotopes. *Geofluids*, **14**, 391–418.

Balsamo, F., Clemenzi, L., Storti, F., Mozafari, M., Solum, J., Swennen, R., Taberner, C. and **Tueckmantel, C.** (2016) Anatomy and paleofluid evolution of laterally restricted extensional fault zones in the Jabal Qusaybah anticline, Salakh arch, Oman. *Geol. Soc. Am. Bull.*, **128**, 957–972.

Banner, J.L. and **Hanson, G.H.** (1990) Calculation of simultaneous isotopic and trace element variations during water-rock interaction with applications to carbonate diagenesis. *Geochim. Cosmochim. Acta*, **54**, 3123–3137.

Beurrier, M., Bechennec, F., Rabu, D. and **Hutin, G.** (1986) *Geologic Map of Rustaq. Sheet NF40-3D. Scale 1:100.000.* Explanatory notes. Directorate General of Minerals, Oman Ministry of Petroleum and Minerals.

Bodin, S., Fiet, N., Godet, A., Matera, V., Westermann, S., Clement, A., Janssen, N.M.M., Stille, P. and **Föllmi, K.B.** (2009) Early Cretaceous (late Berriasian to early Aptian) palaeoceanographic change along the northwestern Tethyan margin (Vocontian Trough, southeastern France): delta C-13, delta O-18 and Sr-isotope belemnite and whole-rock records. *Cretaceous Res.*, **30**, 1247–1262.

Bodin, S., Meissner, P., Janssen, N.M.M., Steuber, T. and **Mutterlose, J.** (2015) Large igneous provinces and organic carbon burial: controls on global temperature and continental weathering during the Early Cretaceous. *Global Planet. Change*, **133**, 238–253.

Bover-Arnal, T., Moreno-Bedmar, J.A., Frijia, G., Pascual-Cebrian, E. and **Ramon Salas, R.** (2016) Chronostratigraphy of the Barremian-Early Albian of the Maestrat Basin (E Iberian Peninsula): integrating strontium-isotope stratigraphy and ammonoid biostratigraphy. *Newsl. Stratigr.*, **49**, 41–68.

vanBuchem, F., Al-Husseini, M.I., Maurer, F., Droste, H.J. and **Yose, L.A.** (2010) Sequence-stratigraphic synthesis of the Barremian – Aptian of the eastern Arabian Plate and implications for the petroleum habitat. In: *Barremian – Aptian Stratigraphy and Hydrocarbon Habitat of the Eastern Arabian Plate* (Eds van Buchem F.S.P., M.I. Al-Husseini, F. Maurer and H.J. Droste), *GeoArabia Spec. Publ.*, **4**, 9–48.

van Buchem, F., Pittet, B., Hillgartner, H., Grotsch, J., Al Mansouri, A.I., Billing, I.M., Droste, H.J. and **Oterdoom, W.H.** (2002) High-resolution sequence stratigraphic architecture of Barremian/Aptian carbonate systems in northern Oman and the United Arab Emirates (Kharaib and Shu'aiba Formations). *GeoArabia*, **7**, 461–500.

Burla, S., Heimhofer, U., Hochuli, P.A., Weissert, H. and **Skelton, P.** (2008) Changes in sedimentary patterns of coastal and deep sea successions from the North Atlantic (Portugal) linked to Early Cretaceous environmental change. *Palaeogeogr. Palaeoclimatol. Palaeoecol.*, **257**, 38–57.

Burla, S., Oberli, F., Heimhofer, U., Wiechert, U. and **Weissert, H.** (2009) Improved time control on Cretaceous coastal deposits: new results from Sr isotope measurements using laser ablation. *Terra Nova*, **21**, 401–409.

Busnardo, R. (1965) Le stratotype du Barrémien. 1.-Lithologie et macrofaune. *Mém. Bur. Rech. Géol. Min.*, **34**, 101–116.

de Caritat, P. and **Baker, J.C.** (1992) Oxygen-isotope evidence for upward, cross-formational porewatcr flow in a sedimentary basin near maximum burial. *Sed. Geol.*, **78**, 155–164.

Choquette, P.W. and **James, N.P.** (1987) Diagenesis 12: diagenesis in limestones – 3. The deep burial environment. *Geosci. Can.*, **14**, 3–35.

Christ, N., Immenhauser, A., Amour, F., Mutti, M., Preston, R., Whitaker, F.F., Peterhänsel, A., Egenhoff, S.O., Dunn, P.A. and **Agar, S.M.** (2012) Triassic Latemar cycle tops – subaerial exposure of platform carbonates under tropical arid climate. *Sed. Geol.*, **265–266**, 1–29.

Clayton, C.J. (1994) Microbial and organic processes. In: *Quantitative Diagenesis: Recent Developments and Applications to Reservoir Geology* (Eds A. Parker and B.W. Sellwood), NATO ASI Series, **453**, 125–160. Springer, Dordrecht.

Coimbra, R. and **Olóriz, F.** (2012a) Pixel counting for percentage estimation: applications to sedimentary petrology. *Comput. Geosci.*, **42**, 212–216.

Coimbra, R. and **Olóriz, F.** (2012b) Contrast comparison of differential diagenetic pathways of Lower Tithonian carbonate materials from the Betic Cordillera (S. Spain): evidence for physico-chemical paleo-seawater properties. *Palaeogeogr. Palaeoclimatol. Palaeoecol.*, **321–322**, 65–79.

Coimbra, R., Immenhauser, A. and **Olóriz, F.** (2009) Matrix micrite $\delta^{13}C$ and $\delta^{18}O$ reveals synsedimentary marine lithification in Upper Jurassic Ammonitico Rosso limestones (Betic Cordillera, SE Spain). *Sed. Geol.*, **219**, 332–348.

Coimbra, R., Azerêdo, A.C., Cabral, M.C. and **Immenhauser, A.** (2016) Palaeoenvironmental analysis of mid-Cretaceous coastal lagoonal deposits (Lusitanian Basin, W Portugal). *Palaeogeogr. Palaeoclimatol. Palaeoecol.*, **446**, 308–325.

Dansgaard, W. (1964) Stable isotopes in precipitation. *Tellus*, **16**, 436–468.

Di Lucia, M., Trecalli, A., Mutti, M. and **Parente, M.** (2012) Bio-chemostratigraphy of the Barremian-Aptian shallow-water carbonates of the southern Apennines (Italy): pinpointing the OAE1a in a Tethyan carbonate platform. *Solid Earth*, **3**, 1–28.

Dunham, R.J. (1962) Classification of carbonate rocks according to their depositional texture. In: *Classification of Carbonate Rocks* (Ed. W.E. Ham), *AAPG Mem.*, **1**, 108–121.

Elrick, M., Roberto Molina-Garza, R., Duncan, R. and **Snow, L.** (2009) C-isotope stratigraphy and paleoenvironmental changes across OAE2 (mid-Cretaceous) from shallow-water platform carbonates of southern Mexico. *Earth Planet. Sci. Lett.*, **277**, 295–306.

El-Sabbagh, A., Tantawy, A., Keller, G., Khozyem, H., Spangenberg, J., Adatte, T. and **Gertsch, B.** (2011) Stratigraphy of the Cenomanian-Turonian oceanic anoxic event OAE2 in shallow shelf sequences of NE Egypt. *Cretaceous Res.*, **32**, 705–722.

Embry, A.F., III and **Klovan, J.E.** (1971) A Late Devonian reef tract on Northeastern Banks Island, NWT. *Bull. Can. Petrol. Geol.*, **19**, 730–781.

Emrich, K., Ehhalt, D.H. and **Vogel, J.C.** (1970) Carbon isotope fractionation during the precipitation of calcium carbonate. *Earth Planet. Sci. Lett.*, **8**, 363–371.

Ferreri, V., Weissert, H., D'Argenio, B. and **Buonocunto, F.P.** (1997) Carbon isotope stratigraphy: a tool for basin to carbonate platform correlation. *Terra Nova*, **9**, 57–61.

Föllmi, K.B. (2012) Early Cretaceous life, climate and anoxia. *Cretaceous Res.*, **35**, 230–257.

Föllmi, K.B., Weissert, H., Bisping, M. and **Funk, H.** (1994) Phosphogenesis, carbon-isotope stratigraphy, and carbonate-platform evolution along the Lower Cretaceous northern Tethyan margin. *Geol. Soc. Am. Bull.*, **106**, 729–746.

Föllmi, K.B., Godet, A., Bodin, S. and **Linder, P.** (2006) Interactions between environmental change and shallow-water carbonate buildup along the northern Tethyan margin and their impact on the Early Cretaceous carbon isotope record. *Paleoceanography*, **21**, 4211–4216, PA4211.

Fournier, M., Lepvrier, C., Razin, P. and **Jolivet, L.** (2006) Late Cretaceous to Paleogene Post-obduction extension and subsequent Neogene compression in Oman Mountains. *GeoArabia*, **11**, 17–40.

Frank, T.D. and **Lohmann, K.C.** (1996) Diagenesis of fibrous magnesian calcite marine cement: implications for the interpretation of $\delta^{18}O$ and $\delta^{13}C$ values of ancient equivalents. *Geochim. Cosmochim. Acta*, **60**, 2427–2436.

Frazer, M., Whitaker, F. and **Hollis, C.** (2014) Fluid expulsion from overpressured basins: implications for Pb-Zn mineralisation and dolomitisation of the East Midlands Platform, northern England. *Mar. Pet. Geol.*, **55**, 68–86.

Frijia, G. and **Parente, M.** (2008) Strontium isotope stratigraphy in the upper Cenomanian shallow-water carbonates of the southern Apennines: short-term perturbations of marine $^{87}Sr/^{86}Sr$ during the oceanic anoxic event 2. *Palaeogeogr. Palaeoclimatol. Palaeoecol.*, **261**, 15–29.

Frijia, G., Parente, M., Di Lucia, M. and **Mutti, M.** (2015) Carbon and strontium isotope stratigraphy of the Upper Cretaceous (Cenomanian-Campanian) shallow-water carbonates of southern Italy: chronostratigraphic calibration of larger foraminifera biostratigraphy. *Cretaceous Res.*, **53**, 110–139.

Glennie, K.W., Boeuf, M.G.A., Hughes-Clarke, M.W., Moody-Stuart, M., Pilaar, W. and **Reinhardt, B.M.** (1974) Geology of the Oman Mountains. *Verh. K. Ned. Geol. Mijnbouw. Genoot.*, **50**, 1–423.

Godet, A., Bodin, S., Föllmi, K.B., Vermeulen, J., Gardin, S., Fiet, N., Adatte, T., Berner, Z., Stüben, D. and **Van de Schootbrugge, B.** (2006) Evolution of the marine stable carbon-isotope record during the early Cretaceous: a focus on the late Hauterivian and Barremian in the Tethyan realm. *Earth Planet. Sci. Lett.*, **242**, 254–271.

Godet, A., Bodin, S., Adatte, T. and **Föllmi, K.B.** (2008) Platform-induced clay-mineral fractionation along a northern Tethyan basin-platform transect: implications for

the interpretation of Early Cretaceous climate change (late Hauterivian-early Aptian). *Cretaceous Res.*, **29**, 830–847.

Godet, A., Durlet, C., Spangenberg, J.E. and **Föllmi, K.B.** (2016) Estimating the impact of early diagenesis on isotope records in shallow-marine carbonates: a case study from the Urgonian platform in western Swiss Jura. *Palaeogeogr. Palaeoclimatol. Palaeoecol.*, **454**, 125–138.

Grötsch, J., Billing, I. and **Vahrenkamp, V.** (1998) Carbon-isotope stratigraphy in shallow-water carbonates: implications for Cretaceous black-shale deposition. *Sedimentology*, **45**, 623–634.

Hanna, S.S. (1990) The Alpine deformation of the Central Oman Mountains. *Geol. Soc. London. Spec. Publ.*, **49**, 341–359.

Harris, P.M., Frost, S.H., Seiglie, G.A. and **Schneidermann, N.** (1984) Regional unconformities and depositional cycles, Cretaceous of the Arabian Peninsula. In: *Interregional Unconformities and Hydrocarbon Accumulation* (Ed. J.S. Schlee), *AAPG Mem.*, **36**, 67–80.

Hassan, K. (2011) Note on the stable isotope values of vein calcite in the El-Seboah peralkaline granite (SW Egypt). *Mineralogia*, **42**, 113–120.

Heimhofer, U., Hochuli, P.A., Burla, S., Oberli, F., Adatte, T., Dinis, J.L. and **Weissert, H.** (2012) Climate and vegetation history of western Portugal inferred from Albian nearshore deposits (Galé Formation, Lusitanian Basin). *Geol. Mag.*, **149**, 1046–1064.

Hendry, J.P. (2002) Geochemical trends and palaeohydrological significance of shallow burial calcite and ankerite cements in Middle Jurassic strata on the East Midlands Shelf (onshore UK). *Sed. Geol.*, **151**, 149–176.

Hillgärtner, H., van Buchem, F., Gaumet, F., Razin, P., Pittet, B., Grötsch, J. and **Droste, H.J.** (2003) The Barremian-Aptian evolution of the eastern Arabian carbonate platform margin (northern Oman). *J. Sed. Res.*, **73**, 756–773.

van Hinsbergen, D.J.J., de Groot, L.V., van Schaik, S.J., Spakman, W., Bijl, P.K., Sluijs, A., Langereis, C.G. and **Brinkhuis, H.** (2015) A paleolatitude calculator for paleoclimate studies. *PLoS ONE*, **10**, e0126946.

Horikx, M., Heimhofer, U., Dinis, J. and **Huck, S.** (2014) Integrated stratigraphy of shallow marine Albian strata in the southern Lusitanian Basin of Portugal. *Newsl. Stratigr.*, **47**, 85–106.

Howarth, R.J. and **McArthur, J.M.** (1997) Statistics for strontium isotope stratigraphy: a robust LOWESS fit to the marine Sr-isotope curve for 0 to 206 Ma, with look-up table for derivation of numeric age. *J. Geol.*, **105**, 441–456.

Huck, S. and **Heimhofer, U.** (2015) Improving shallow-water carbonate chemostratigraphy by means of rudist bivalve sclerochemistry. *Geochem. Geophys. Geosyst.*, **16**, 3111–3128.

Huck, S., Rameil, N., Korbar, T., Heimhofer, U., Wieczorek, T.D. and **Immenhauser, A.** (2010) Latitudinally different responses of Tethyan shoal-water carbonate systems to the Early Aptian oceanic anoxic event (OAE 1a). *Sedimentology*, **57**, 1585–1614.

Huck, S., Heimhofer, U., Rameil, N., Bodin, S. and **Immenhauser, A.** (2011) Strontium and carbon-isotope chronostratigraphy of Barremian-Aptian shoal-water carbonates: Northern Tethyan platform drowning predates OAE1a. *Earth Planet. Sci. Lett.*, **304**, 547–558.

Huck, S., Heimhofer, U. and **Immenhauser, A.** (2012) Early Aptian algal bloom in a neritic proto-North Atlantic setting: Harbinger of global change related to OAE1a? *Geol. Soc. Am. Bull.*, **124**, 1810–1825.

Huck, S., Heimhofer, U., Immenhauser, A. and **Weissert, H.** (2013) Carbon-isotope stratigraphy of Early Cretaceous (Urgonian) shoal-water deposits: Diachronous changes in carbonate-platform production in the north-western Tethys. *Sed. Geol.*, **290**, 157–174.

Huck, S., Stein, M., Immenhauser, A., Skelton, P.W., Christ, N., Föllmi, K.B. and **Heimhofer, U.** (2014) Response of proto-North Atlantic carbonate platform ecosystems to OAE1a-related stressors. *Sed. Geol.*, **313**, 15–31.

Hughes-Clarke, M.W. (1988) Stratigraphy and rockunit nomenclature in the oil-producing area of interior Oman. *J. Petrol. Geol.*, **11**, 5–60.

Immenhauser, A., Kenter, J.A.M., Ganssen, G., Bahamonde, J.R., van Vliet, A. and **Saher, M.H.** (2002) Origin and significance of isotope shifts in Pennsylvanian carbonates (Asturias, NW Spain). *J. Sed. Res.*, **72**, 82–94.

Immenhauser, A., Hillgärtner, H., Sattler, U., Bertotti, B., Schoepfer, P., Homewood, P., Vahrenkamp, V., Steuber, T., Masse, J.-P., Droste, H.H.J., van Koppen, J., van der Kooij, B., van Bentum, E.C., Verwer, K., Hoogerduijn-Strating, E., Swinkels, W., Peters, P., Immenhauser-Potthast, I. and **Al Maskery, S.A.J.** (2004) Barremian-lower Aptian Qishn Formation, Haushi-Huqf area, Oman: a new outcrop analogue for the Kharaib/Shu'aiba reservoirs. *GeoArabia*, **9**, 153–194.

Immenhauser, A., Hillgärtner, H. and **van Bentum, E.** (2005) Microbial-foraminiferal episodes in the Early Aptian of the southern Tethyan margin: ecological significance and possible relation to oceanic anoxic event 1a. *Sedimentology*, **52**, 77–99.

Immenhauser, A., Holmden, C. and **Patterson, W.P.** (2008) Interpreting the carbon-isotope record of ancient shallow epeiric seas: lessons from the recent. In: *Dynamics of Epeiric Seas* (Eds B.R. Pratt and C. Holmden), *Geol. Assoc. Canada Spec. Publ.*, **48**, 135–174.

Jenkyns, H.C. (1995) Carbon-isotope stratigraphy and paleoceanographic significance of the Lower Cretaceous shallow-water carbonates of Resolution Guyot, Mid-Pacific Mountains. *Proc. ODP Sci. Res.*, **143**, 99–108.

van der Kooij, B., Immenhauser, A., Csoma, A., Bahamonde, J. and **Steuber, T.** (2009) Spatial geochemistry of a Carboniferous platform-margin-to-basin transect: balancing environmental and diagenetic factors. *Sed. Geol.*, **219**, 136–150.

Krencker, F.-N., Bodin, S., Hoffmann, R., Suan, G., Mattioli, E., Kabiri, L., Föllmi, K.B. and **Immenhauser, A.** (2014) The middle Toarcian cold snap: trigger of mass extinction and carbonate factory demise. *Global Planet. Change*, **117**, 64–78.

Le Metour, J., Villey, M. and **de Gramont, X.** (1986) *Geologic Map of Masqat, sheet NF-40-4D, scale 1:100,000, with Explanatory Notes*. Directorate General of Minerals, Ministry of Petroleum and Minerals, Oman.

Lohmann, K.C. (1988) Geochemical patterns of meteoric diagenetic systems and their application to studies of Paleokarst. In: *Paleokarst* (Eds N.P. James and P.W. Choquette), pp. 58–80. Springer-Verlag, Berlin.

Malkoč, M. and **Mutterlose, J.** (2010) The early Barremian warm pulse and the late Barremian cooling: a high resolution geochemical record of the Boreal Realm. *Palaios*, **25**, 14–23.

Marshall, J.D. (1992) Climatic and oceanographic isotopic signals from the carbonate rock record and their preservation. *Geol. Mag.*, **129**, 143–160.

Masse, J.-P., Borgomano, J. and **Al Maskiry, S.** (1998a) A platform-to-basin transition for lower Aptian carbonates (Shuaiba Formation) of the northeastern Jebel Akhdar (Sultanate of Oman). *Sed. Geol.*, **119**, 297–309.

Masse, J.-P., Chartrousse, A. and **Borgomano, J.** (1998b) The lower Cretaceous (Upper Barremian-Lower Aptian) caprinid rudists from Northern Oman. *Geobios Mem. Spec.*, **22**, 211–223.

McArthur, J.M., Howarth, R.J.and **Bailey, T.R.** (2001) Strontium Isotope Stratigraphy: LOWESS Version 3: best fit to the marine Sr-Isotope Curve for 0–509 Ma and accompanying look-up table for deriving numerical age. *J. Geol.* **109**, 155–170.

Menegatti, A.P., Weissert, H., Brown, R.S., Tyson, R.V., Farrimond, P., Strasser, A. and **Caron, M.** (1998) High-resolution $\delta^{13}C$ stratigraphy through the early Aptian "Livello Selli" of the Alpine Tethys. *Paleoceanography*, **13**, 530–545.

Meyers, W.J. and **Lohmann, K.C.** (1985) Isotope geochemistry of regionally extensive calcite cement zones and marine components in Mississippian limestones, New Mexico. In: *Carbonate Cements* (Eds N. Schneidermann and P.M. Harris), *SEPM Spec. Publ.*, **26**, 223–239.

Millán, M.I., Weissert, H.J., Fernández-Mendiola, P.A. and **García-Mondéjar, J.** (2009) Impact of Early Aptian carbon cycle perturbations on evolution of a marine shelf system in the Basque-Cantabrian Basin (Aralar, N Spain). *Earth Planet. Sci. Lett.*, **287**, 392–401.

Millán, M.I., Weissert, H.J., Owen, H., Fernández-Mendiola, P.A. and **García-Mondéjar, J.** (2011) The Madotz Urgonian platform (Aralar, northern Spain): paleoecological changes in response to Early Aptian global environmental events. *Palaeogeogr. Palaeoclimatol. Palaeoecol.*, **312**, 167–180.

Moore, C.H. (1985) Upper Jurassic subsurface cements: a case history. In: *Carbonate Cements* (Eds P.M. Hams and N. Schneidermann). *SEPM Spec. Publ.*, **36**, 291–308.

Morad, S., Al-Aasm, I.S., Sirat, M. and **Sattar, M.M.** (2010) Vein calcite in cretaceous carbonate reservoirs of Abu Dhabi: record of origin of fluids and diagenetic conditions. *J. Geochem. Explor.*, **106**, 156–170.

Moss, S. and **Tucker, M.E.** (1995) Diagenesis of Barremian-Aptian platform carbonates (the Urgonian Limestone Formation of SE France): near-surface and shallow-burial diagenesis. *Sedimentology*, **42**, 853–874.

Mozafari, M., Swennen, R., Balsamo, F., Clemenzi, L., Storti, F., El Desouky, H.A., Tueckmantel, C., Solum, J. and **Taberner, C.** (2015) Paleofluid evolution in fault-damage zones: evidences from fault-fold interaction events in the Jabal Qusaybah anticline (Adam Foothills, North Oman). *J. Sed. Res.*, **85**, 1525–1551.

Parente, M., Frijia, G. and **Di Lucia, M.** (2007) Carbon-isotope stratigraphy of Cenomanian-Turonian platform carbonates from southern Apennines (Italy): a chemostratigraphic approach to the problem of correlation between shallow-water and deep-water successions. *J. Geol. Soc.*, **164**, 609–620.

Patterson, W.P. and **Walter, L.M.** (1994) Syndepositional diagenesis of modern platform carbonates: evidence from isotopic and minor element data. *Geology*, **22**, 127–130.

Pittet, B., Van Buchem, F.S.P., Hillgärtner, H., Razin, P., Grötsch, J. and **Droste, H.** (2002) Ecological succession, paleoenvironmental change, and depositional sequences of Barremian-Aptian shallow-water carbonates in northern Oman. *Sedimentology*, **49**, 555–581.

Prokoph, A., Shields, G.A. and **Veizer, J.** (2008) Compilation and timeseries analysis of a marine carbonate $\delta^{18}O$, $\delta^{13}C$, $^{87}Sr/^{86}Sr$ and $\delta^{34}S$ database through Earth history. *Earth-Sci. Rev.*, **87**, 113–133.

Rameil, N., Immenhauser, A., Csoma, A.E. and **Warrlich, G.** (2012) Surfaces with a long history: the Aptian top Shu'aiba Formation unconformity, Sultanate of Oman. *Sedimentology*, **59**, 212–248.

Ruffell, A.H. and **Batten, D.J.** (1990) The Barremian-Aptian arid phase in western Europe. *Palaeogeogr. Palaeoclimatol. Palaeoecol.*, **80**, 197–212.

Sanders, D. (2003) Syndepositional dissolution of calcium carbonate in neritic carbonate environments: geological recognition, processes, potential significance. *J. Afr. Earth Sci.*, **36**, 99–134.

Sattler, U., Immenhauser, A., Hillgärtner, H. and **Esteban, M.** (2005) Characterization, lateral variability and lateral extent of discontinuity surfaces on a carbonate platform (Barremian to Lower Aptian, Oman). *Sedimentology*, **52**, 339–361.

Schöne, B.R. (2008) The curse of physiology – challenges and opportunities in the interpretation of geochemical data from mollusk shells. *Geo-Mar. Lett.*, **28**, 269–285.

Schröder, R., van Buchem, F.S.P., Cherchi, A., Baghbani, D., Vincent, B., Immenhauser, A. and **Granier, B.** (2010) Revised orbitolinid biostratigraphic zonation for the

Barremian – Aptian of the eastern Arabian Plate and implications for regional stratigraphic correlations. In: *Barremian – Aptian Stratigraphy and Hydrocarbon Habitat of the Eastern Arabian Plate* (Eds van Buchem F.S.P., M.I. Al-Husseini, F. Maurer and H.J. Droste), *GeoArabia Spec. Publ.*, **4**, 49–96.

Sharland, P.R., Archer, R., Casey, D.M., Davies, R.B., Hall, S.H., Heward, A.P., Horbury, A.D. and **Simmons, M.D.** (2001) Sequence Stratigraphy of the Arabian Plate. *GeoArabia Spec. Publ.*, **2**, 371.

Shemesh, A., Ron, H., Erel, Y., Kolodny, Y. and **Nur, A.** (1992) Isotopic composition of vein calcite and its fluid inclusions: implication to paleohydrological systems, tectonic events and vein formation processes. *Chem. Geol.*, **94**, 307–314.

Simmons, M.D. (1990) *Aspects of the Micropalaeontology and Stratigraphy of Cretaceous Shelf Carhonates from the Oman Mountains*. Unpublished PhD thesis, Council for National Academic Awards, 279 pp.

Simmons, M.D. (1994) Micropalaeontological biozonation of the Kahmah Group (Early Cretaceous), Central Oman Mountains. In: *Micropalaeontology and Hydrocarbon Exploration in the Middle East* (Ed. M.D. Simmons), *Br. Micropalaeontol. Soc. Publ. Ser.*, Chapman and Hall, London, 177–220.

Simmons, M.D. and **Hart, M.B.** (1987) The biostratigraphy and microfacies of the Early to Mid-Cretaceous of Wadi Mi'aidin, Central Oman Mountains. In: *Micropalaeontology of Carbonate Environments* (Ed. M.B. Hart), pp. 176–207. Ellis Horwood, Chichester, UK.

Sprovieri, M., Coccioni, R., Lirer, F., Pelosi, N. and **Lozar, F.** (2006) Orbital tuning of a lower Cretaceous composite record (Maiolica Formation, central Italy). *Paleoceanography*, **21**, PA4212.

Stein, M., Föllmi, K.B., Westermann, S., Godet, A., Adatte, T., Matera, V., Fleitmann, D. and **Berner, Z.** (2011) Progressive palaeoenvironmental change during the Late Barremian-Early Aptian as prelude to Oceanic Anoxic Event 1a: evidence from the Gorgo a Cerbara section (Umbria-Marche basin, central Italy). *Palaeogeogr. Palaeoclimatol. Palaeoecol.*, **302**, 396–406.

Strasser, A. (2015) Hiatuses and condensation: an estimation of time lost on a shallow carbonate platform. *Depositional Rec.*, **1**, 91–117.

Strohmenger, C.J., Ghani, A., Al-Jeelani, O., Al-Mansoori, A., Al-Dayyani, T., Weber, L.J., Al-Mehsin, K., Vaughan, L., Kahn, S.A. and **Mitchell, J.C.** (2006) High resolution sequence stratigraphy and reservoir characterization of Upper Thamama (Lower Cretacesous) reservoirs of a giant Abu Dhabi oil field, United Arab Emirates. In: *Giant Hydrocarbon Reservoirs of the World: From Rocks to Reservoir Characterization and Modeling* (Eds P.M. Harris and L.J. Weber), *Am. Assoc. Petrol. Geol. Mem., SEPM Spec. Publ.*, **88**, 139–171.

Vandeginste, V., John, C.M. and **Manning, C.** (2013) Interplay between depositional facies, diagenesis and early fractures in the Early Cretaceous Habshan Formation, Jebel Madar, Oman. *Mar. Pet. Geol.*, **43**, 489–503.

Veizer, J., Ala, D., Azmy, K., Bruckschen, P., Buhl, D., Bruhn, F., Carden, G.A.F., Diener, A., Ebneth, S., Godderis, Y., Jasper, T., Korte, C., Pawellek, S., Podlaha, O.G. and **Strauss, H.** (1999) ^{87}Sr, $\delta^{13}C$ and $\delta^{18}O$ evolution of Phanerozoic seawater. *Chem. Geol.*, **161**, 59–88.

Vincent, B., Brigaud, B., Emmanuel, L. and **Loreau, J.-P.** (2017) High resolution ion microprobe investigation of the $\delta^{18}O$ of carbonate cements (Jurassic, Paris Basin, France): new insights and pending questions. *Sed. Geol.*, **350**, 42–54.

Walter, L.M., Ku, T.C.W., Muehlenbachs, K., Patterson, W.P. and **Bonnell, L.** (2007) Controls on the $\delta^{13}C$ of dissolved inorganic carbon in marine pore waters: an integrated case study of isotope exhange during syndepositional recrystallization of biogenic carbonate sediments (South Florida Platform, USA). *Deep Sea Res. Part II*, **54**, 1163–1200.

Weissert, H. and **Erba, E.** (2004) Volcanism, CO_2 and paleoclimate: a Late Jurassic-Early Cretaceous oxygen isotope record. *J. Geol. Soc.*, **161**, 695–702.

Weissert, H., McKenzie, J.A. and **Channell, J.E.T.** (1985) Natural variations in the carbon cycle during the Early Cretaceous. In: *The Carbon Cycle and Atmospheric CO_2: Natural Variations Archean to the Present* (Eds E.T. Sundquist and W.S. Broecker), *AGU Geophys. Monogr.*, **32**, 531–545.

Weissert, H., Joachimski, M.M. and **Sarnthein, M.** (2008) Chemostratigraphy. *Newsl. Stratigr.*, **42**, 145–179.

Wilson, H.H. (1969) Late Cretaceous eugeosynclinal sedimentation, gravity tectonics, and ophiolite emplacement in Oman Mountains, Southeast Arabia. *AAPG Bull.*, **53**, 626–652.

Wissler, L., Weissert, H., Masse, J.-P. and **Bulot, L.G.** (2002) Chemostratigraphic correlation of Barremian and lower Aptian ammonite zones and magnetic reversals. *Int. J. Earth Sci.*, **91**, 272–279.

Witt, W. and **Gökdag, H.** (1994) Orbitolinid biostratigraphy of the Shu'aiba Formation (Aptian), Oman – implications for reservoir development. In: *Micropalaeontology and Hydrocarbon Exploration in the Middle East* (Ed. M.D. Simmons), *Br. Micropalaeontol. Soc. Publ. Ser.*, Chapman and Hall, London, 221–242.

Wohlwend, S., Hart, M. and **Weissert, H.** (2016) Chemostratigraphy of the Upper Albian to mid-Turonian Natih Formation (Oman) – how authigenic carbonate changes a global pattern. *Depositional Rec.*, **2**, 97–117.

Wohlwend, S., Celestino, R., Reháková, D., Huck, S. and **Weissert, H.** (2017) Late Jurassic to Cretaceous evolution of the eastern Tethyan Hawasina Basin (Oman Mountains). *Sedimentology*, **64**, 87–110.

Supporting Information

Additional Supporting Information may be found online in the supporting information tab for this article:

Table S1. Bulk carbonate carbon- and oxygen isotope results (Jabal Madar section).

Table S2. Component-specific carbon- and oxygen isotope variability (Jabal Madar).

Table S3. De-dolomite contents and stable isotope data of selected subsamples (Jabal Madar).